REPORT DOCUMENTATION PAGE

AFRL-SR-AR-TR-03-
0051

Public reporting burden for this collection of information is estimated to average 1 hour per response, including ... ces, gathering and maintaining the data needed, and completing and reviewing the collection of information. Send c ... this collection of information, including suggestions for reducing this burden, to Washington Headquarters Services, ... son Davis Highway, Suite 1204, Arlington, VA 22202-4302, and to the Office of Management and Budget, Paperwork R...

1. AGENCY USE ONLY (*Leave Blank*)

2. REPORT DATE
February 8, 2003

3. REPORT TYPE
Final Report 8 November 2001 to 8 November 2002

4. TITLE AND SUBTITLE
Continuously Tunable 3-5 μm Single-Frequency Laser source

5. FUNDING NUMBERS
Contract # F49620-01-C-0003

6. AUTHORS
Ramon U. Martinelli

7. PERFORMING ORGANIZATION NAME(S) AND ADDRESS(ES)
Sarnoff Corporation
201 Washington Road
Princeton, NJ 08540

8. PERFORMING ORGANIZATION REPORT NUMBER

9. SPONSORING / MONITORING AGENCY NAME(S) AND ADDRESS(ES)

LTC John C. Carrano	LTC Todd Steiner
DARPA/MTO	United States Air Force Office of Scientific Research
3701 North Fairfax Drive	801 N. Randolph Street
Arlington, VA 222203-1714	Arlington, VA 22203

10. SPONSORING / MONITORING AGENCY REPORT NUMBER

11. SUPPLEMENTARY NOTES

In collaboration with Naval Research Laboratory, Optical Sciences Division.

12a. DISTRIBUTION / AVAILABILITY STATEMENT

Distribution Statement A. Approved for public release; distribution is unlimited.

12b. DISTRIBUTION CODE

13. ABSTRACT (*Maximum 200 words*)

The goal of this project is to develop a 3-5 μm continuously tunable single-frequency laser source. Our approach uses an external cavity (EC) and various tuning elements in conjunction with a semiconductor optical amplifier (SOA). Optically pumped, amorphous-silicon ridge-waveguide lasers, grown via molecular-beam epitaxy, were developed that could function as curved-ridge-waveguide SOAs. The lasers operate at a temperature of 295 K, where they output 7 mW per facet. The wavelength is 3 μm. Comparison with a stripe laser in the same material suggests that a flaw in the ridge metal mask induces losses that increase the threshold pump power and similarly reduce the external efficiency. The lateral far-field for the ridge-waveguide lasers are multi-lobed, indicating that the lasers are not operating in the fundamental lateral mode.

Sarnoff designed and constructed an EC that is compatible with the use the SOAs. The EC is 8 cm long with a footprint less than 1 ft^2. Sarnoff designed, fabricated and partially characterized the tuning etalon that selects one longitudinal cavity mode. It is an air-gap etalon using silicon-based mirrors and a 16.5-μm-thick polycarbonate spacer ring. The etalon free spectral range is 9 THz, which is the estimated SOA gain width.

14. SUBJECT TERMS
tunable lasers, mid-infrared diode lasers, semiconductor optical amplifier, antimonide-based lasers, external cavity, external-cavity laser, tuning etalon

15. NUMBER OF PAGES
56

16. PRICE CODE

17. SECURITY CLASSIFICATION OF REPORT	18. SECURITY CLASSIFICATION OF THIS PAGE	19. SECURITY CLASSIFICATION OF ABSTRACT	20. LIMITATION OF ABSTRACT
Unclassified	Unclassified	Unclassified	SAR

NSN 7540-01-280-5500

Standard Form 298 (Rev. 2-89)
Prescribed by ANSI Std. Z39-1
298-102

20030306 058

Table of Contents

I. **Introduction** 1

Goals and Applications 1

Approach 1

II. **The Semiconductor Optical Amplifier (SOA)** 3

Design 3

Electrically Pumped SOA 3

Optically Pumped SOA 6

The Physical Structure of the SOA 6

Curved Ridge Waveguide 7

The Minimum Radius of Curvature for the Curved Ridge Waveguide 7

III. **Experimental Results for the Semiconductor Optical Amplifier** 9

Lincoln Laboratory Optically Pumped SOA Structure and Processing 9

Sarnoff SOA Processing 10

Photoluminescence Calibration and Characterization of Sarnoff SOAs 13

Amorphous Silicon (a-Si) Ridge Waveguides 18

Characterization of a-Si-Coated Optically Pumped 3.2-μm Lasers 20

MBE Growth and Characterization of Additional Sarnoff SOAs 27

Description of a-Si Ridge Waveguide Processing 28

Laser Results on a-Si Straight/Normal Ridge Waveguides 30

SOA Summary and Conclusions 32

IV. **External Cavity Calculations and Experiments** 33

The External Cavity Laser: General Considerations 33

Diffraction Grating as a Tuning Etalon 37

Tuning Etalon Design 38

External Cavity and Components 40

Coarse-Tuning Etalon Measurements 42

External Cavity Summary and Conclusions 46

V. **Summary** 46

VI. **References** 47

Figures

Figure 1. The essential elements of the tunable external cavity laser.....1

Figure 2. The schematic mode spectra of the external cavity (**red**) and the coarse-tuning etalon (**blue**), along with the gain spectrum of the semiconductor optical amplifier (**black**). 2

Figure 3. Energy-band diagram of a W-QW laser. 3

Figure 4. W-QW band diagram showing the important energy states, along with the electron-hole wavefunction intensity overlap.....4

Figure 5. The layer structure of an electrically pumped 3.3-μm W-QW SOA. 5

Figure 6. Layer structure of an optically pumped optical amplifier (SOA).....6

Figure 7. Schematic of a ridge waveguide that supports the fundamental spatial mode of the SOA. 6

Figure 8. Schematic diagram of a curved ridge waveguide semiconductor optical amplifier.....7

Figure 9. The geometrical configuration of the curved waveguide SOA.....8

Figure 10. Schematic diagram of a RWG comprising an epitaxially grown laser structure with a thin top cladding layer and a deposited dielectric ridge.....9

Figure 11. The vertical structure of Lincoln Laboratory wafer # 299-066, comprising a 6-W-QW gain region between two n-AlGaAsSb cladding layers. The W-QW structure is shown at the right. 10

Figure 12. Optically pumped 3.75-μm antimonide laser with an a-Si 0.4-μm-thick RWG deposited in two different ways.....11

Figure 13. The RWG design for the curved SOA. 11

Figure 14. The layer structure of an optically pumped 3.2-μm W-QW SOA.....12

Figure 15. A schematic diagram of the 3.2-μm 10-W-QW structure with an a-Si ridge waveguide and an SiN_x-metal blocking layer. 13

Figure 16. The layer structure of an optically pumped 3.25-μm W-QW laser, wafer JGK-0090. 14

Figure 17. The PL spectra of wafer JGK-0090 at T = 77, 200, and 300 K.....14

Figure 18. The variation of the PL peak at 300 K with InAs-layer thickness in the W-QWs.....15

Figure 19. The pulsed-mode output-power characteristics taken at 77 K of wafer JGK-0090 coated with electron-beam-deposited Si.....15

Figure 20. The temperature sensitivity of the threshold pump intensity for a laser from wafer JGK-0090.....16

Figure 21. The 78-K output spectrum of a laser from wafer JGK-0090. 17

Figure 22. The 78-K output spectrum of a laser from wafer JGK-0091. 17

Figure 23. A photograph of wafer JGK-0090 partially coated with CVD-deposited Si. The vertical striations are an artifact of the computer-copying-pasting process. 18

Figure 24. Optical absorption coefficient as a function of photon energy for a typical a-Si:H film made by plasma-enhanced chemical-vapor deposition. The sub-bandgap absorption was measured by photo-thermal deflection spectroscopy. The absorption coefficient of crystalline silicon is shown for comparison. 19

Figure 25. (a) Refractive indices of a series of a-SiN_x films made by varying N_2/SiH_4 ratio in the PECVD deposition; (b) refractive indices of a series of a-SiC for films using a gas mixture of SiH_4 + CH_4 + H_2. 20

Figure 26. SEM picture of a cross section of an a-SiN_x ridge waveguide with n = 3.4 made on SiO_2 coated c-Si substrate. An SF_6 plasma was used to etch the waveguide. 20

Figure 27. Layer structure of wafers JGK0116 and JGK0150 coated after MBE growth with 0.8 μm of Si. 21

Figure 28. Output-power characteristics of an optically pumped laser from JGK0116 at four temperatures. 22

Figure 29. Output-power characteristics of an optically pumped laser from JGK0150 at four temperatures. 22

Figure 30. The exponential increase of the threshold power with increasing temperature for devices 116. 23

Figure 31. The exponential increase of the threshold power with increasing temperature for devices 150. 23

Figure 32. The decrease of the external efficiency with increasing temperature of 3 lasers from 116 unit incident pump power. Note that in terms of photons out per facet per incident pump photon, η_d = 0.012 at 78 K, which is threefold higher than the slope efficiency in W/W. 24

Figure 33. The decrease of the external efficiency with increasing temperature of 3 lasers from 150. 24

Figure 34. The external efficiency at 78 K for lasers at 0.5-mm intervals along the bar from JGK0116. 25

Figure 35. The external efficiency at 78 K for lasers at 0.5-mm intervals along the bar from 150. 25

Figure 36. The output spectra of a laser from 116 at six different temperatures. 26

Figure 37. The output spectra of a laser from 150 at six different temperatures. 26

Figure 38. The temperature dependence of the wavelength of lasers from 116. 27

Figure 39. The layer structure of an optically pumped 3.25-μm W-QW laser (JGK0234). 27

Figure 40. The structure of GaSb-waveguide 3.25-μm W-QW laser......28
Figure 41. Schematic diagram of the a-Si ridge waveguide......28
Figure 42. SEM images of metal 2-μm overlap of a-Si ridge waveguide......29
Figure 43. Output-power characteristics for an optically pumped straight/normal a-Si RWG on laser wafer JGK0150 at a temperature of 295 K......30
Figure 44. The temperature dependence of the threshold current for RWG and non-RWG lasers from wafer JGK0150......31
Figure 45. Lateral far-field pattern for a 7-μm-wide a-Si RWG on wafer JGK0150. 31
Figure 46. Lateral far-field pattern for a 12-μm-wide a-Si RWG on wafer JGK0150......32
Figure 47. The essential elements of the tunable external cavity laser......33
Figure 48. The schematic mode spectra of the external cavity and the coarse-tuning etalon, along with the gain spectrum of the semiconductor optical amplifier......34
Figure 49. Etalon finesse needed to select a single longitudinal cavity mode. Etalon free spectral range is chosen to be 320 nm (9.4 THz), or equal to a gain-bandwidth of 10% of the optical frequency, which corresponds to a wavelength of 3.2 μm......35
Figure 50. Corresponding mirror reflectivity needed to achieve etalon Finesse shown in Figure 49......35
Figure 51. Schematic of solid (left) and air-gap (right) etalon. A ring spacer, such as ultra-low-expansion quartz, is used to set air-gap spacing......35
Figure 52. Wavelength tuning by etalon rotation. At ten-degrees rotation (off normal), the etalon transmission peak sweeps through one free-spectral range. The etalon is formed by a 16 μm air-gap between two HR/AR-coated ZnSe plates. The total external-cavity length has to be adjusted to maintain fixed cavity modes as etalon is rotated. Mounting the cavity end-mirror on a piezo actuator provides the needed length control, a total displacement of 1.6 μm (i.e. $\lambda_0/2$)......36
Figure 53. Etalon finesse increases with mirror reflectivity......37
Figure 54. Schematic of grating-tuned external cavity laser. Under the Littrow configuration and for a given wavelength, the angle of diffraction equals the angle of incidence. 38
Figure 55. Littrow angles, θ_L, as a function of grating groove density for a variety of center wavelengths. 38
Figure 56. Tuning etalon fabrication process. 39
Figure 57. Fabricating the etalon with wedged substrates prevents cavity filter effects from other points in the construct. The white lines represent proper etalon transmission. The black lines show the lateral and angular drift of the beam when reflecting off the AR-coated surfaces......40

Figure 58. External Cavity Design (Note: all components are to scale except the SOA and lenses which are shown larger to be easily discernable)..................... 41

Figure 59. Etalon mask showing the round windows for the optical cavity and the avenues for sawing the wafer. 42

Figure 60. Tuning etalon clamp design.. 43

Figure 61. FTIR transmittance spectrum of a tuning etalon with a polycarbonate spacer. FTIR resolution is 2 cm^{-1}.. 44

Figure 62. FTIR transmittance versus wavenumber of an etalon with polycarbonate spacer. FTIR resolution is 2 cm^{-1}.. 44

Figure 63. Etalon transmission spectrum similar to those in Figures 61 and 62, but with mirrors adjusted to be more nearly parallel.. 45

Figure 64. Least-squares fit of etalon peak-transmission wavenumber versus half-wavelength number.. 45

I. Introduction

Goals and Applications

The goal of this project is to develop a 3- to 5-μm continuously tunable single-frequency laser source. Such a device has many uses valuable to DoD:

- Compact wavelength-agile sources in chem-bio sensors aboard unmanned vehicles or in a ground-based trace-gas monitoring system.
- Narrow-linewidth wavelength-agile sources to seed high-power pulsed 3-5 μm OPO LIDAR for remote chem-bio and aerosol detection.
- The illuminator in a 3-5 μm imaging system that monitors trace gases in the volume of a scene to establish the levels of danger present.
- The 3-5 μm source in portable breath analyzers that helps determine a wounded soldier's condition.
- The agile single-frequency source for secure battlefield free-space communications.

Commercial applications include trace-gas monitoring [1], free-space communications, and medical diagnostics through human breath analysis [2-4].

Approach

Our approach uses an external cavity (EC) and various tuning elements in conjunction with a semiconducting optical amplifier (SOA) that provides two-pass optical gain. Figure 1 shows the schematic diagram of the tunable external cavity laser (ECL).

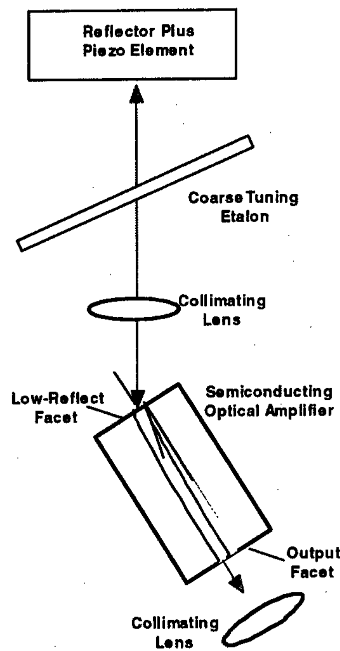

Figure 1. The essential elements of the tunable external cavity laser.

The SOAs are antimonide-based W-quantum-well (W-QW) lasers [5] with the facet internal to the cavity having a very low reflectivity (< 10^{-4}). This low reflectivity is achieved, in part, by having a curved ridge waveguide that meets the facet at an angle of about 6° off the normal [6-8]. The low facet reflectivity inhibits laser oscillations within the SOA. Because the curved ridge waveguide meets the low-reflect facet at an angle of 6°, optical refraction dictates that the beam inside the EC meets the low-reflect facet of the SOA at an angle of about 20°. The SOA provides two-pass optical gain.

The SOA output facet is normal to the waveguide and forms one end of the external cavity. The output facet has a reflectivity of 30 to 50%. A reflecting mirror that is micro-positioned longitudinally by a piezo-electric element forms the other end of the cavity. A coarse tuning etalon selects a single longitudinal cavity mode that lies within the SOA gain curve. Along with collimating lenses, these components form a tunable external-cavity laser. To tune over the entire range from 3 to 5 μm, several ECLs may be used.

Coordinated adjustments of the coarse-tuning element and the piezo-electric element that drives the retro-reflector accomplish mode selection in the ECL. Figure 2 illustrates the process. Three sets of curves are shown: the comb of modes associated with the external cavity defined by the retro-reflector and the output-facet of the SOA (**red**); the modes of the coarse-tuning etalon, which is a relatively high-finesse etalon (**blue**); and the gain profile of the SOA (**black**), all as a function of wavelength. Note that the mode spacing of the etalon need not be, and probably will not be, an integer multiple of the EC mode spacing.

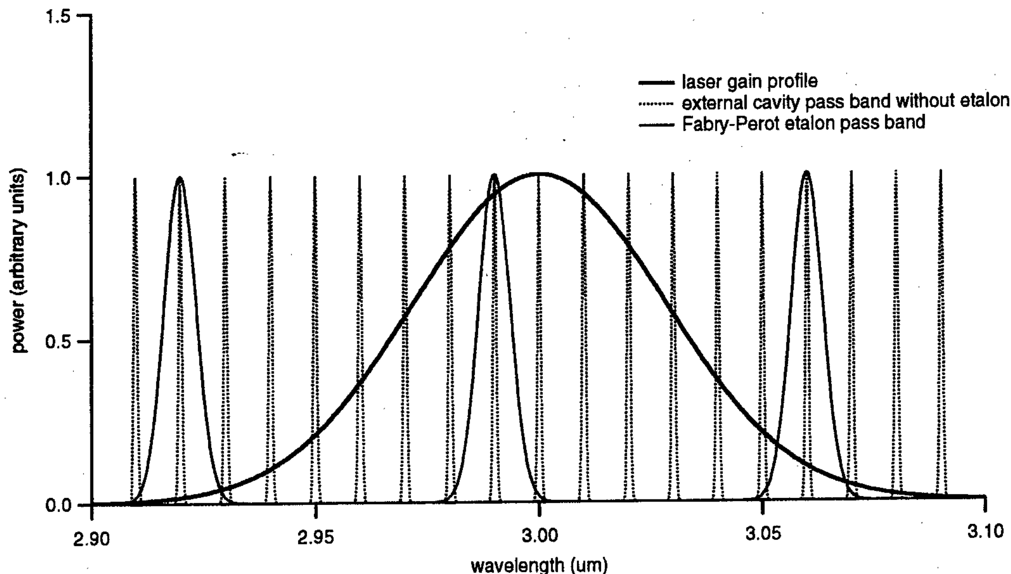

Figure 2. The schematic mode spectra of the external cavity ***(red)*** *and the coarse-tuning etalon* ***(blue)****, along with the gain spectrum of the semiconductor optical amplifier* ***(black)****.*

A particular ECL mode is selected by tuning the peak of the coarse-tuning etalon pass-band to correspond with the peak of an external-cavity mode that lies sufficiently near the maximum of the gain profile to generate lasing. The coarse-tuning element is a Fabry-Perot etalon with a free spectral range about equal to the optical gain halfwidth. By synchronizing the tuning of the retro-reflector/piezo and the coarse-tuning etalon, the ECL output

wavelength can be continuously swept through the useable portion of the SOA gain spectrum, which should be 300 to 400 nm, depending on the external-cavity optical losses and the SOA center wavelength. The temperature of the SOA can be changed to shift the SOA gain peak, and hence, extend the ECL wavelength range.

Using SOAs with gain spectra distributed throughout the 3 – 5 μm optical interval, and designing the elements of the EC to operate within the gain spectrum of the SOA, single-frequency laser sources can be realized.

As a member of the team, Dr. Jerry Meyer and his group at The Naval Research Laboratory (NRL) designed the SOAs in consultation with Sarnoff. Sarnoff grew and fabricated the SOAs, and the NRL characterized them. SOA wafers were also supplied by MIT Lincoln Laboratories. The curved ridge waveguide was designed at Sarnoff with inputs from NRL. Sarnoff designed, fabricated and tested the EC.

In this report we discuss the design, fabrication and testing of the SOA and the EC. Following these presentations, we summarize our results and give our conclusions.

II. The Semiconductor Optical Amplifier (SOA)

Design

The SOA is a mid-infrared laser that has, as mentioned above, a very low reflectivity at the facet internal to the external cavity. Otherwise, it is identical to a laser. In this project the SOA uses W-QWs as the optical gain media. The W-QWs are pumped either electrically or optically. Since optical pumping is relatively easier to achieve, our first SOAs are optically pumped.

Electrically Pumped SOA

Figure 3 shows the generic energy-band diagram of an electrically pumped W-QW diode laser [5].

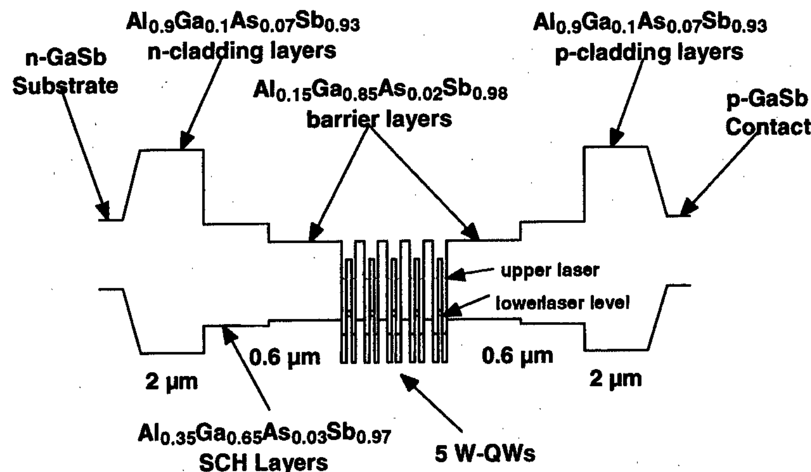

Figure 3. Energy-band diagram of a W-QW laser.

All SOA structures are grown by molecular-beam epitaxy (MBE). Beginning with an n-GaSb substrate, the composition is graded to $Al_{0.9}Ga_{0.1}As_{0.07}Sb_{0.93}$, which is the 2-μm-thick

n-cladding layer. The graded region is as heavily Te-doped as possible (i. e., about 2 x 10^{17} cm^{-3}) to reduce Ohmic losses. The separate-confinement heterostructure (SCH) layer is grown next. The SCH layers are 0.6-μm thick and are designed to confine the optical mode to the waveguide region consisting of the SCH/W-QW/SCH layers, with only a small percentage of the mode in the more heavily doped cladding layers. Thus, optical losses resulting mainly from free-carrier absorption are greatly reduced. This design approach was developed at Sarnoff and is known as the broadened-waveguide design [9]. The SCH layer may have two compositions, as shown in Figure 3, or it may comprise a single-composition AlGaAsSb layer, the Al-composition of which is about 35%. The energy barriers in a step-graded SCH layer tend to force carriers into the W-QWs, increasing the internal efficiency.

A number of identical W-QWs are grown next. In searching for the optimal gain, this number varies from 3 to 10. The thicknesses and compositions of the wells determine the peak optical gain position. The structure is completed by growing symmetrical SCH, p-cladding, p-graded, and p-GaSb cap layers. The p-type dopant is Be.

In some designs we have inserted a superlattice, "hole-blocker", at the n-cladding/SCH interface. This superlattice has a forbidden band at the n-cladding valence band edge that impedes hole injection from the SCH into the n-cladding layer. Thus, holes are more strongly confined to the waveguide region, increasing the laser's internal efficiency [10].

A detailed energy-band diagram of three W-QWs is shown in Figure 4. Also shown is the overlap of the intensities of the electron and hole wavefunctions.

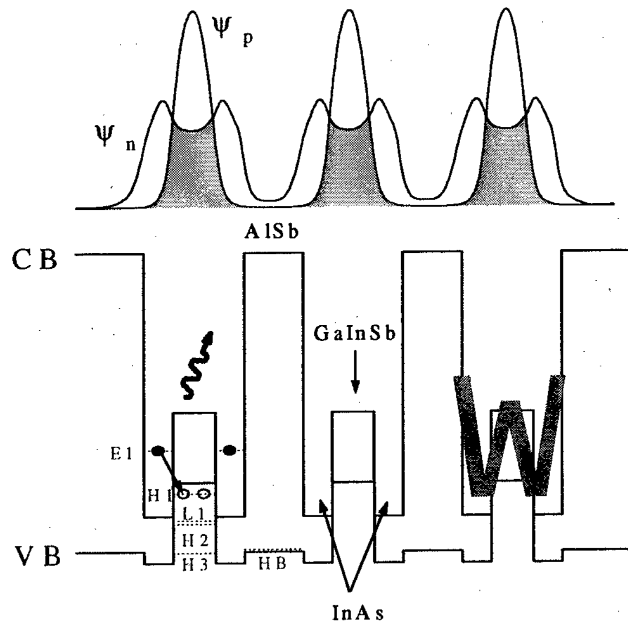

Figure 4. W-QW band diagram showing the important energy states, along with the electron-hole wavefunction intensity overlap.

The W-QWs employed in our lasers comprise two InAs layers sandwiching a GaInSb layer. The QW barriers shown in Figure 4 are AlSb, but in many of our devices the barriers have

been AlGaAsSb having the same composition as the SCH layer. Typical thicknesses of the W-QW components are 3.2 nm for the AlSb, 1.7 nm for the InAs, and 3.0 nm for the GaInSb. The name W-QW comes from the obvious similarity of the energy-band diagram of the quantum well to the letter W.

As shown in Figure 4, the W-QWs are type-II, and the lasing transition, E_1 to H_1, has a diagonal component. The transition is from the first electron state, E_1, in the InAs to the first heavy-hole state, H_1, in the GaInSb. The symmetrical nature of the W-QW increases the electron-hole wavefunction overlap, and hence, the gain. Nonetheless, the diagonal nature of the transition reduces the gain by about 50%, compared with that of a type-I QW. Auger recombination in a W-QW is, however, only one-sixth that of a comparable type-I QW [11, 12]. This is critical in mid-infrared lasers, for Auger recombination rates increase exponentially with increasing wavelength and with increasing temperature. Large Auger recombination rates translate into high threshold currents and low maximum-operating temperatures.

Details of the 3.3-μm (T = 300 K) electrically pumped SOA layer structure are shown in Figure 5.

Region	Composition	Thickness	Doping	Optical Confinement	Repeat	λ = 3.3 μm			
Cap layer	p^+-GaSb	50 nm	2.0E+19		1				
Transition	Graded p-AlGaAsSb	50 nm	5.0E+18		1				
p-clad	p-$Al_{0.9}Ga_{0.1}As_{0.07}Sb_{0.93}$	1.5 μm	5.0E+18	0.09	1				
SCH	$Al_{0.35}Ga_{0.65}As_{0.03}Sb_{0.97}$	0.6 μm	undoped	0.30	1				
1st Barrier	$Al_{0.15}Ga_{0.85}As_{0.05}Sb_{0.95}$	80 Å	undoped		1				
W-Active	InAs/GaInSb/InAs/AlGaAsSb W	0.14 μm	undoped	0.15		InAs	$Ga_{0.75}In_{0.25}Sb$	InAs	$Al_{0.15}Ga_{0.85}As_{0.05}Sb_{0.95}$
					x 5	15 Å	27 Å	15 Å	80 Å
Hole blocker	InAs/AlSb	20 nm	undoped	0.10		InAs	AlSb		
					x 11	10 Å	9 Å		
SCH	$Al_{0.35}Ga_{0.65}As_{0.03}Sb_{0.97}$	0.6 μm	undoped	0.28					
n-clad	n-$Al_{0.9}Ga_{0.1}As_{0.07}Sb_{0.93}$	2.0 μm	5.00E+17	0.09	1				
Transition	Graded n-AlGaAsSb	50 nm	5.00E+17		1				
Buffer	n-GaSb								
Substrate	n-GaSb								

Figure 5. The layer structure of an electrically pumped 3.3-μm W-QW SOA.

The layer structure is given from the p-GaSb cap layer down to the substrate. The composition, thickness and doping levels are given in the second, third, and fourth columns. The cladding layers are 1.5-μm thick. Using Te as the n-type dopant limits the doping of the n-type layers to about 2×10^{17} cm^{-3}, whereas the p-AlGaAsSb layers can be doped to 5×10^{18} cm^{-3}. The maximum doping level in n-AlGaAsSb is compensated by the order-of-magnitude larger electron mobility in AlGaAsSb, as compared with hole mobility in p-AlGaAsSb, thus rendering resistivities of n- and p-AlGaAsSb nearly equal. The waveguide region is undoped. The AlGaAsSb SCH layers have an Al-content of 35%.

The present design calls for 5 W-QWs. The thickness and composition of each constituent is given in columns 7 through 10. The number of QWs and the width of the SCH layers may be varied to optimize performance. The hole-blocker superlattice comprises eleven undoped layers each of InAs (10 Å) and AlSb (9 Å).

Optically Pumped SOA

The layer structure of the optically pumped SOA [12] is shown in Figure 6.

Layer	Structure	Thickness (Å)	Repeats	Index					
Top Clad	$AlAs_{0.08}Sb_{0.92}$	6000	1	3.18	To define 5-um-wide ridge waveguide: etch 4500 Å of top clad, dep				
					InAs	GaSb	InAs	AlSb	
Active	InAs/GaSb/InAs/AlSb W	960	10	3.49	17 Å	30 Å	17 Å	32 Å	(confinement factor = 11%)
Hole Blocker	$AlAs_{0.08}Sb_{0.92}$	100	1	3.18					
SCH	GaSb	3000	1	3.73					
Bottom Clad	$AlAs_{0.08}Sb_{0.92}$	20000	1	3.18					
Substrate	GaSb	500 μm		3.73					
	Total MBE Thickness (μm)	3.006							
	Designed for emission at 3.2 um at 300 K			Modal Index = 3.32					

Figure 6. Layer structure of an optically pumped optical amplifier (SOA).

This structure is designed to operate at 3.2 μm at 300 K. Because there is no carrier transport through the cladding layers, the entire structure is intentionally undoped. This reduces free-carrier absorption in the cladding layers. Electron-hole pairs are generated directly in the W-QWs by absorbing 1-μm or 2-μm pump radiation. To increase absorption, there are 10 W-QWs in the optically pumped structure. The overlap of the optical mode with the W-QWs, also called the confinement factor, Γ, is 11%. The value of Γ in near-infrared QW lasers normally about 1%; so we have designed a strong coupling between the mode and the W-QWs to decrease the threshold pump radiation power. However, W-QWs introduce losses stemming from interface-roughness scattering and free-carrier absorption. It is unclear what the optimal number of W-QWs is. We varied the number of W-QWs to see how it affects performance in terms of threshold pump power, SOA efficiency and tuning range.

The Physical Structure of the SOA

To guide the wave in the lateral direction, a 0.4-μm-high ridge will be etched in the chip as indicated schematically in Figure 7. The ridge width at its base is 3 to 5 μm. It provides weak index guiding that supports only the zero-order lateral mode. This waveguide has also been formed by an etched ridge of amorphous silicon (a-Si) that has been deposited on top of the wafer.

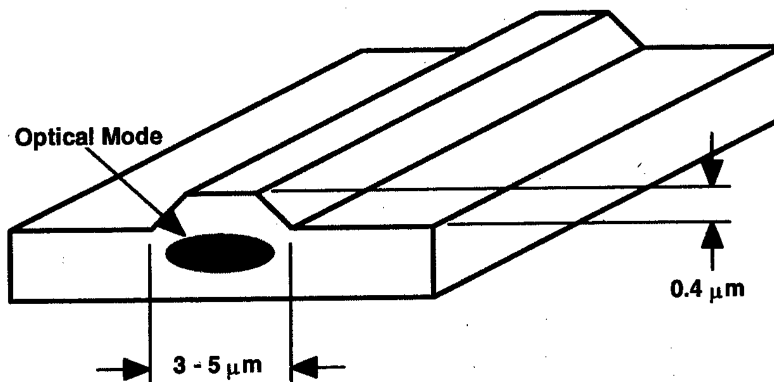

Figure 7. Schematic of a ridge waveguide that supports the fundamental spatial mode of the SOA.

Curved Ridge Waveguide

As discussed above, the SOA incorporates a curved ridge waveguide. A schematic diagram of the curved ridge waveguide is shown in Figure 8.

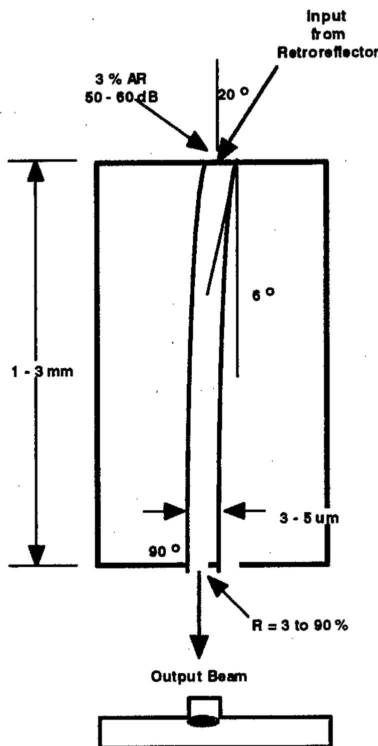

Figure 8. Schematic diagram of a curved ridge waveguide semiconductor optical amplifier.

The ridge meets the output facet at 90°, and the reflectivity, R, of the facet is a design variable. The facet is coated so that R = 30%. The ridge meets the opposite facet at an angle of 6°, and the facet is coated with a standard quarter-wave Al_2O_3 layer that results in a reflectivity of about 3%. The effective reflectivity at this facet is less than 10^{-4} [6]. The optical beam enters and exits this facet at about 20°.

For electrical pumping, the entire chip area, including the ridge, is coated with an insulator, a contact stripe is opened along the ridge, and a Ti/Pt/Au Ohmic metallization layer is deposited. In the case of optical pumping, the ridge is defined as before, but no contact opening is made. Metal is deposited everywhere *except* on top of the ridge, thus acting as a mask for pump radiation. Pump radiation is only absorbed beneath the ridge, and hence only along the curved ridge is there optical gain. The metal mask inhibits Fabry-Perot laser action between the parallel facets of the chip.

The Minimum Radius of Curvature for the Curved Ridge Waveguide

Figure 9 shows schematically, and not to scale, the plan view of the curved ridge waveguide SOA.

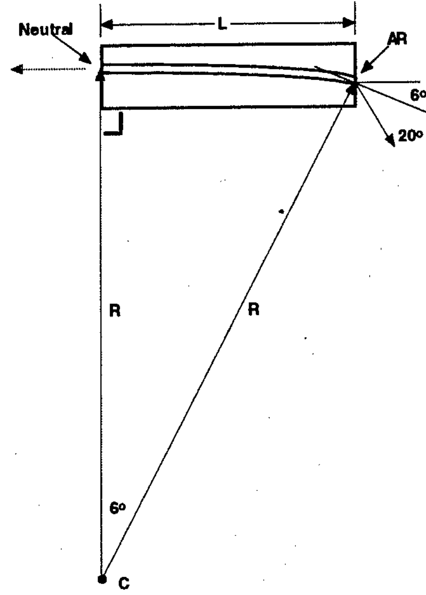

Figure 9. The geometrical configuration of the curved waveguide SOA.

The ridge is an arc of a circle that is perpendicular to the output facet of the SOA. This output facet has a neutral optical coating that reflects about 30% of the modal power back into the SOA. The other end of the ridge meets the low-reflect (3%) facet at an angle of about 6°. This means that the output beam is refracted from the normal by about 20°, because the effective refractive index of the optical mode in the SOA is about 3.4. The combination of the angled ridge and the low-reflect facet coating makes the modal reflectivity at this facet less than 10^{-4} [6]. There is, therefore, little concern with etalons set up within the ECL through reflections off this facet. Neither do we expect laser oscillation to occur within the SOA. Coupling efficiencies of about 50% have been measured from angled ridge waveguides into a collimating lens [G. Alphonse of Sarnoff Corporation, private communication]. The design shown in Figure 9 maximizes the arc's radius of curvature, R. The SOA cavity length is L.

The fundamental mode in a curved ridge waveguide experiences radiation losses [7, 8]. There is an evanescent portion of the mode, extending radially outward from the ridge that attains a phase velocity exceeding the speed of light in the semiconductor. The optical power in this portion radiates away and is lost.

Below is an expression that gives the minimum radius of curvature, R, of the ridge waveguide, as shown in Figure 9, for which losses are negligible. This formula is derived from Equation (21) of reference [7].

$$R \geq \frac{n_e^2 \lambda}{\left(n_e^2 - n_c^2\right)^{\frac{3}{2}}}$$

The free-space wavelength is λ, and it is about 3 μm. The modal refractive index is n_e and is about 3.4. The refractive index in the channels adjacent to the ridge is n_c, and the difference

between n_e and n_c is about 0.003. Consequently, the channels and the ridge form a weak dielectric waveguide that supports only the fundamental lateral optical mode. Using these parameter values, we find that for a ridge radius of curvature $R \geq 1.2$ cm, radiation losses are negligible.

From the geometry of Figure 9, the arc of the ridge subtends about 0.1 radian, and L is approximately equal to the arc length, so $L \approx 0.1\ R = 1.2$ mm. A minimum chip or cavity length of 1.2 mm is practical. Mid-IR lasers with cavity lengths as long as 2 to 3 mm have shown excellent performance, especially if internal optical losses are about 2 cm^{-1} [9].

The curved ridge waveguide can be designed to have negligible radiation losses. For $\lambda = 3\ \mu m$, the design limits the ridge or cavity length to a minimum of about 1.2 mm, which is a very practical value. For $\lambda = 5\ \mu m$ the cavity length increases to 2 mm, still a practical value.

III. Experimental Results for the Semiconductor Optical Amplifier

Lincoln Laboratory Optically Pumped SOA Structure and Processing

Early in the project, Sarnoff lost its only MBE grower. To maintain continuity in the program, Sarnoff received permission to obtain SOA structures from Dr. George Turner of MIT Lincoln Laboratory. This subsection describes his SOA design and the SOA structures that he supplied to us.

Since optical pumping does not require current flow though the laser, an index-guiding ridge-waveguide (RWG) design can be implemented by depositing a suitable detection, or low-conductivity material on the top of a grown laser structure. This is shown in Figure 10.

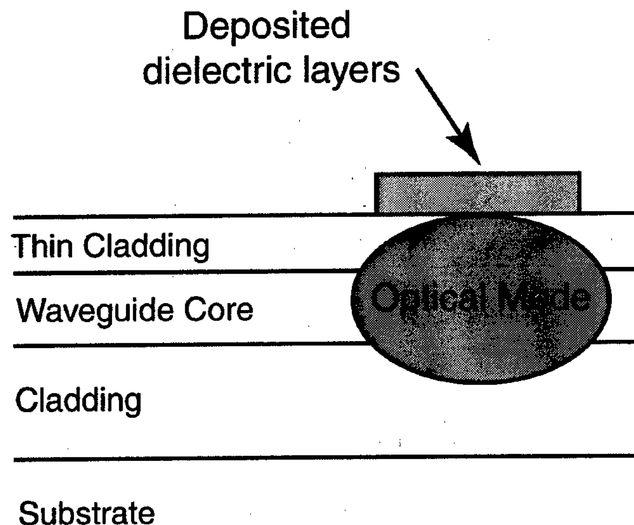

Figure 10. Schematic diagram of a RWG comprising an epitaxially grown laser structure with a thin top cladding layer and a deposited dielectric ridge

This innovative design comes from Dr. George Turner's group at Lincoln Laboratory (LL). The top cladding layer is thinner than normal: 0.1 μm as opposed to the usual thickness of

about 2 μm. The deposited dielectric is about 0.4 μm thick and is chosen to be transparent and lossless at the lasing wavelength. The RWG width is 5 to 10 μm, and it is designed to support the fundamental lateral optical mode.

Figure 11 shows the vertical structure of the SOA. It was grown via MBE by the Lincoln Laboratory staff under the direction of Dr. George Turner.

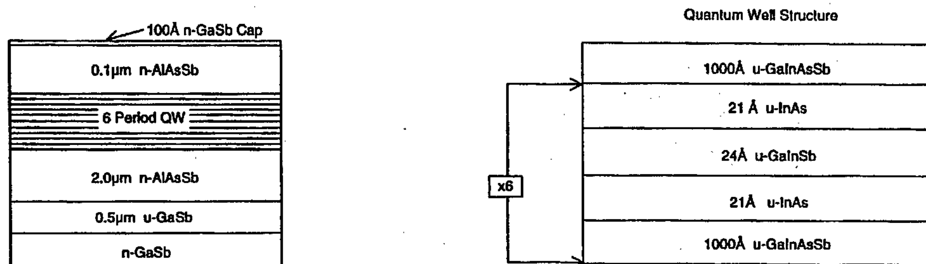

Figure 11. The vertical structure of Lincoln Laboratory wafer # 299-066, comprising a 6-W-QW gain region between two n-AlGaAsSb cladding layers. The W-QW structure is shown at the right.

The 100-Å GaSb cap layer protects the AlGaAsSb from oxidation. The six W-QWs are undoped and the cladding layers are lightly doped n-type. In an optically pumped device there is no need for a p-n junction, and avoiding n- and especially p-doping reduces the optical losses. P-doped antimonides in general have large intervalence-band absorption coefficients in the mid-infrared.

The upper cladding layer is only 0.1 μm thick, whereas the lower cladding layer is 2 μm thick. This is because an amorphous electron-beam-deposited silicon ridge waveguide is deposited on top of the structure to provide index guiding.

A detailed picture of the individual W-QW is shown in Figure 11. The W-QW consists of a 24- Å GaInSb layer between two 21- Å InAs layers. 1000- Å -thick GaInSb barriers separate the wells and absorb pump radiation. The room-temperature lasing wavelength is designed to be 3.75 μm. All the materials comprising the wells and the barriers are undoped.

Sarnoff SOA Processing

Sarnoff processed the SOA in two ways, as shown in Figure 12.

In the first method the amorphous silicon (a-Si) is deposited and defined as a RWG. Then a metallic layer is deposited and defined on the areas adjacent to the ridge. The metal acts as an optical shield; only the region beneath the RWG is optically pumped. This is an important feature in the case of curved waveguides, because the pump beam is in the form of a broad stripe. Without the metal shield Fabry-Perot laser action could occur outside the RWG. The Ti in the metal is likely to present a loss to any part of the mode that interacts with it. However, this may help inhibit lasing in higher order lateral modes.

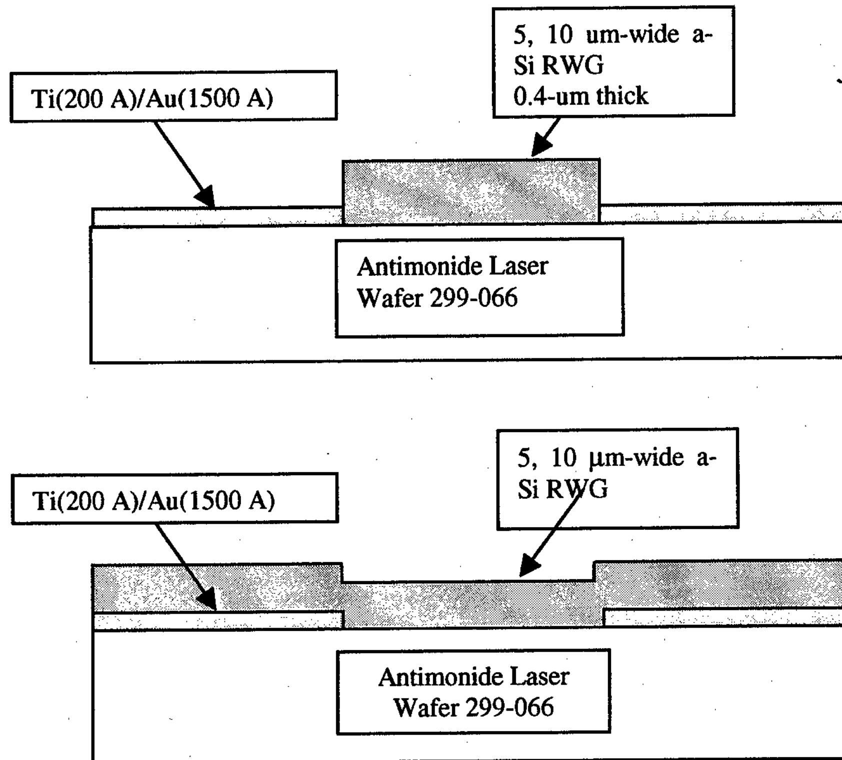

Figure 12. Optically pumped 3.75-μm antimonide laser with an a-Si 0.4-μm-thick RWG *deposited in two different ways.*

Figure 13 shows the curved RWG optically pumped processed using wafer 299-066.

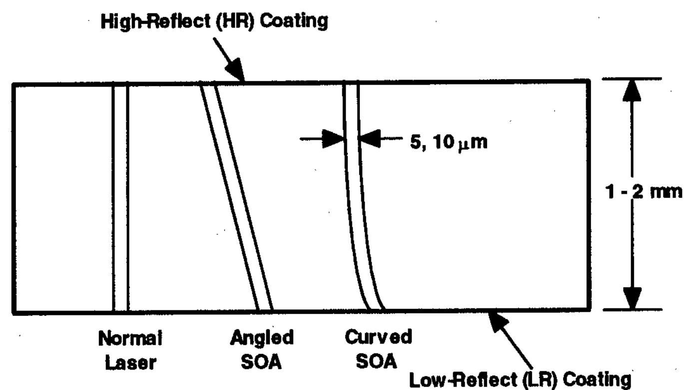

Figure 13. The RWG design for the curved SOA.

The SOAs are of three basic ridge-waveguide designs: a linear RWG aligned perpendicular to the facet plane; a linear, angled RWG that meets both facets at 6° from the normal; and a curved RWG that is normal to the high-reflect (HR) facet plane and is 6° off the normal at the low-reflect (LR) facet plane. The curve of the RWG is a circular arc, as discussed above. The linear RWG perpendicular to the facets is a standard optically pumped RWG laser. It is

used to test the quality of the material and the processing. Its lasing properties, as a function of temperature, assess the quality of the ridge and the losses introduced by the metal shield. The characteristics of the angled linear RWG SOA are compared with the characteristics of the curved RWG. This comparison allows an estimate of the losses from the curvature of the RWG. Cavity lengths of 1 and 2 mm were fabricated, along with RWG widths of 5 and 10 μm. The processed wafer was cleaved into facet-coated and tested 1- and 2-mm-wide bars.

Before cleaving it into bars, Wafer 299-066 was thinned to about 150 μm. Otherwise, cleaving would have been irregular and difficult to control. Because the curved ridge waveguides had to be cleaved at precise locations, we had to assure a controllable cleaving process, which requires pre-thinning the wafer before making bars. This is the standard process for laser fabrication. Once the wafer was thinned, it was cleaved into 1- and 2-mm bars, HR and LR facet coated, and tested at NRL.

LL also grew 3.2-μm SOAs. The structure of these SOAs is shown in Figure 14.

Layer	Structure	Thickness (Å)	Repeats	Index
Cap Layer	GaSb	100	1	3.73
Top Clad	$Al_{0.5}Ga_{0.5}As_{0.04}Sb_{0.96}$	2000	1	3.45
Active	InAs/GaSb/InAs/AlSb W	960	10	3.49
Hole Blocker	$AlAs_{0.08}Sb_{0.92}$	100	1	3.18
SCH	GaSb	1000	1	3.73
Bottom Clad	$AlAs_{0.08}Sb_{0.92}$	20000	1	3.18
Substrate	GaSb	Thick		3.73

(confinement factor = 13%)

InAs	GaSb	InAs	AlSb
17 Å	30 Å	17 Å	32 Å

Total MBE Thickness (μm) 2.416
Designed for emission at 3.2 um at 300 K
All grown layers are undoped

Figure 14. The layer structure of an optically pumped 3.2-μm W-QW SOA.

This structure has a 10-W-QW active region and a lower GaSb SCH layer. The bottom $AlAs_{0.08}Sb_{0.92}$ cladding layer is 2 μm thick, but the top cladding layer is $Al_{0.5}Ga_{0.5}As_{0.04}Sb_{0.96}$, and it is only 0.2 μm thick. A very thin (10 nm) GaSb cap layer protects the top cladding layer from oxidizing.

A 0.3-μm a-Si ridge waveguide was generated on the top side of the wafer to provide lateral index guiding. A 0.3-μm-thick SiN_x layer with metal on top was deposited everywhere outside the ridge to block the pump laser radiation. The finished chip profile, taken normal to the RWG, is shown schematically in Figure 15.

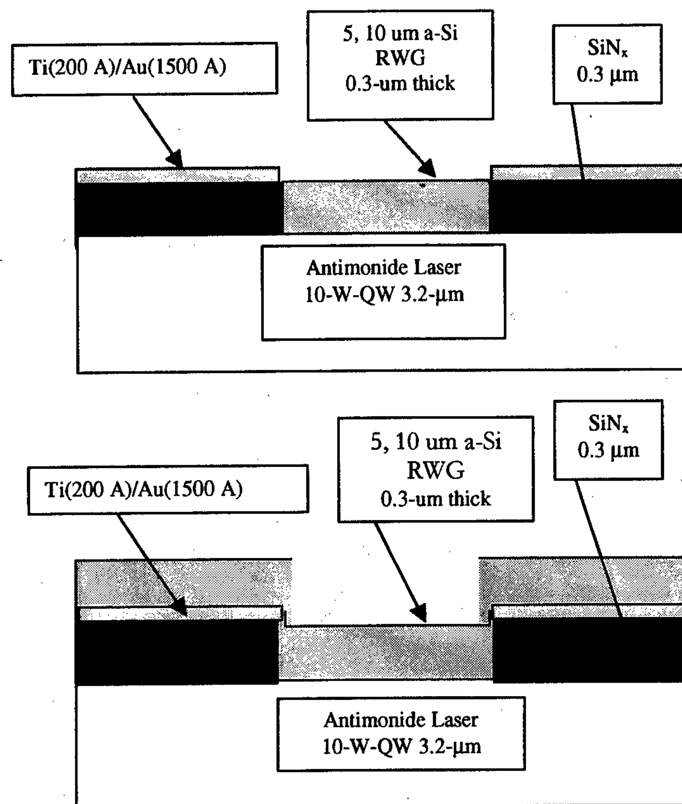

Figure 15. A schematic diagram of the 3.2-µm 10-W-QW structure with an a-Si ridge waveguide and an SiN_x-metal blocking layer.

As was done with wafer 299-066, two approaches were taken. In the first, a 0.3-µm-thick a-Si RWG was defined, and SiN_x was deposited everywhere outside the RWG. An Au optical mask was then deposited on the SiN_x. In the second approach, The SiN_x and the Au were first deposited and defined, and then a-Si was deposited everywhere.

Unfortunately, none of these LL-grown SOA structures exhibited lasing when the perpendicular RWG lasers were tested at NRL. The devices were tested under conditions identical to Sarnoff lasers discussed in Section IV.

Photoluminescence Calibration and Characterization of Sarnoff SOAs

Sarnoff grew via MBE seven wafers to calibrate the photoluminescent (PL) wavelength of the W-QW optically pumped laser structure. The goal was to determine the W-QW configuration that gave a lasing wavelength of about 3.2 µm at room temperature. The basic structure is shown in Figure 16.

Structure of JGK-0090								
Layer	**Structure**	**Thickness (nm)**	**Repeats**	**Index (3.25 um)**				
Cap	GaSb	10	1	3.73				
Hole Blocker	$AlAs_{0.08}Sb_{0.92}$	10	1	3.18				
					InAs	GaSb	InAs	AlSb
Active W-QW	InAs/GaSb/InAs/AlSb W	96	10	3.49	19.7 Å	30 Å	19.7 Å	35 Å
Hole Blocker	$AlAs_{0.08}Sb_{0.92}$	10	1	3.18				
SCH	GaSb	100	1	3.73				
Bottom Clad	$AlAs_{0.08}Sb_{0.92}$	2000	1	3.18				
Buffer	GaSb	500	1	3.73				
Substrate	GaSb	Thick		3.73				

Figure 16. The layer structure of an optically pumped 3.25-μm W-QW laser, wafer JGK-0090.

The PL spectra of one of the wafers, JGK-0090, taken at 77, 200, and 300 K, are shown in Figure 17.

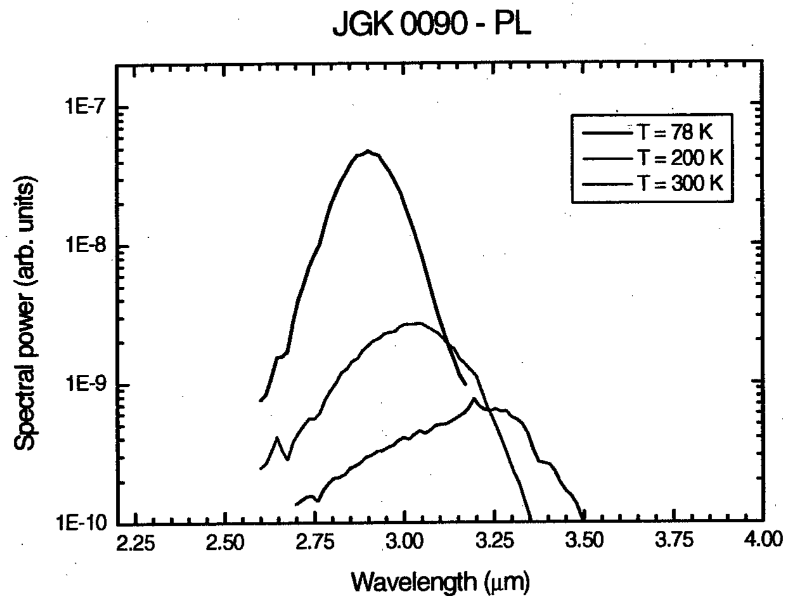

Figure 17. The PL spectra of wafer JGK-0090 at T = 77, 200, and 300 K

At 77 K the PL peaks at about 2.9 μm. With increasing temperature the PL peak diminishes in magnitude and shifts to longer wavelengths, reaching 3.25 μm at 300 K. The average rate of the peak μm shift is 1.6 nm/K. The PL spectrum broadens with increasing temperature, as well. Atmospheric water-vapor absorption produces the structure in the spectra at about 2.7 μm.

To calibrate the MBE growth system, the structure shown in Figure 16 was repeatedly grown varying the thickness of the InAs in every W-QW. PL data were taken, and the variation in the PL peak with InAs-layer thickness. Figure 18 shows the results.

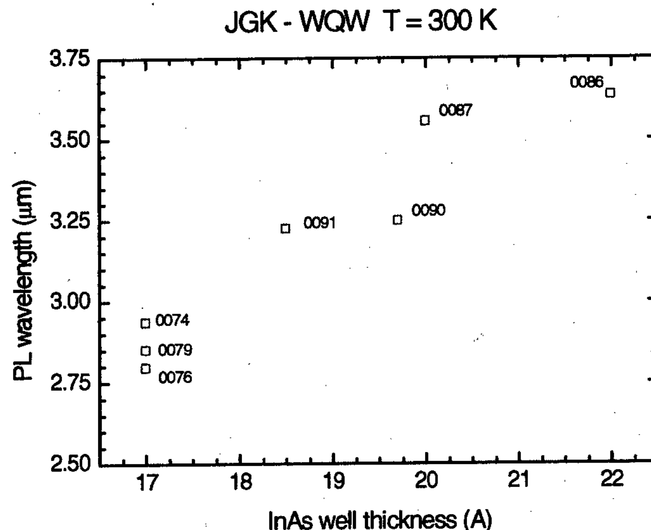

Figure 18. The variation of the PL peak at 300 K with InAs-layer thickness in the W-QWs.

As it turned out, the InAs thickness for wafers JGK-0090 (shown in Figure 16) and JGK-0091 had the right InAs-layer thickness, about 1.95 nm, to produce a 300-K PL at 3.25 μm. Note that the InAs thicknesses plotted in Figure 18 are average values of the InAs-layer thickness, as determined through analysis of the double-crystal X-ray spectra measured for each of these wafers. Figure 18 gives us the calibration required to produce any PL wavelength from 2.8 to 3.6 μm.

Wafers JGK-0090 and JGK-0091 were then coated with 500-nm of electron-beam-deposited Si and shipped to the NRL for characterization as optically pumped lasers without ridge waveguide. The Si acts as the top section of the transverse optical waveguide. Figure 19 shows the pulsed-mode output-power characteristics of wafer JGK-0090.

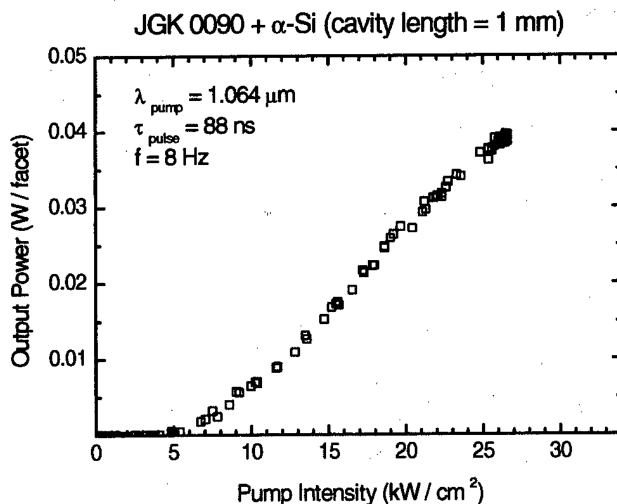

Figure 19. The pulsed-mode output-power characteristics taken at 77 K of wafer JGK-0090 coated with electron-beam-deposited Si.

The wafer was cleaved into bars 1 mm long; the facets were uncoated. The bars were held at 77 K and pumped in the pulsed-mode with a 1.064-μm Nd:YAG laser. The stripe width of the pump low beam was 150 μm, and it was normal to the facets. The pulse width was 88 ns, and the repetition rate was 8 Hz. This translates into a duty cycle of 1 x 10^{-8}, which means that laser heating was negligible. The threshold pump intensity, P_{th}, is about 6 kW/cm^2, which is ten to forty times greater than those of similar devices [12]. This indicated that something was seriously wrong with the wafers. The external power-conversion efficiency is very low at 0.13%. It's typically 3% [12]. Lasers from wafer JGK-0091 exhibited similar behavior.

The increase of the threshold pump intensity with increasing temperature is shown in Figure 20.

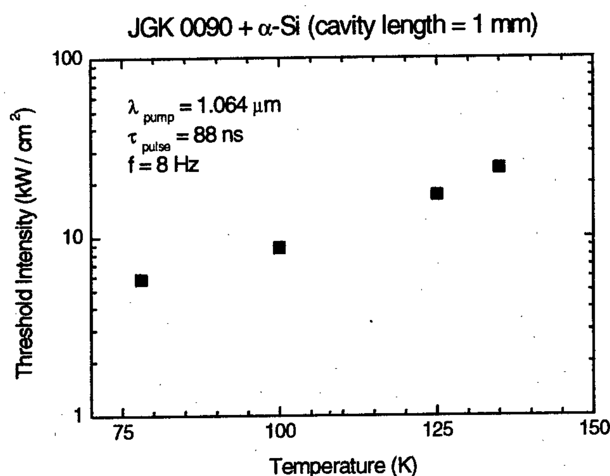

Figure 20. The temperature sensitivity of the threshold pump intensity for a laser from wafer JGK-0090.

The temperature sensitivity of P_{th} increases faster than exponentially with increasing temperature. Using the data points at the three highest temperatures to calculate the characteristic temperature, T_0, one obtains a value of 35 K. This is close to the value obtained for 3.2-μm W-QW diode lasers [5]. The rather temperature-insensitive behavior of the threshold pump intensity near 77 K is most likely the result of P_{th} being so large that it masks any temperature variation.

The lasing spectra from JGK-0090 and -0091 are shown in Figures 21 and 22, respectively.

Referring to Figure 17, the multi-mode spectrum of Figure 21 falls slightly to the short-wavelength side of the PL peak. The PL peak and the lasing wavelength for optically pumped devices occur at about the same wavelength. At room temperature we expect the lasing wavelength to be about 3.2 μm.

During wafer testing, it was noticed that the surfaces of wafers JGK-0090 and –0091 were covered with spots. Figure 23 shows a photograph of the surface of wafer JGK-0090.

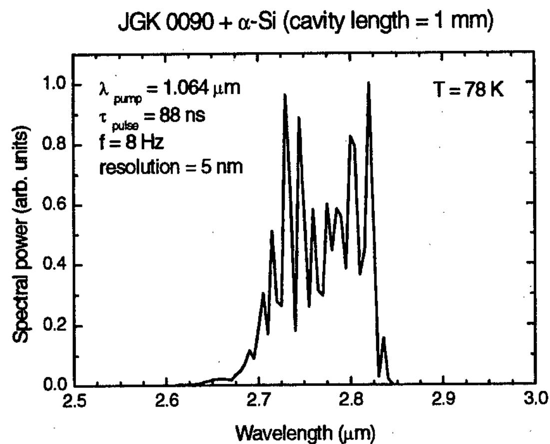

Figure 21. The 78-K output spectrum of a laser from wafer JGK-0090.

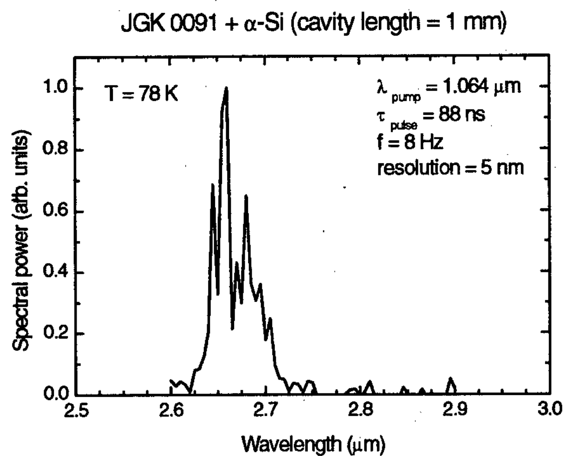

Figure 22. The 78-K output spectrum of a laser from wafer JGK-0091.

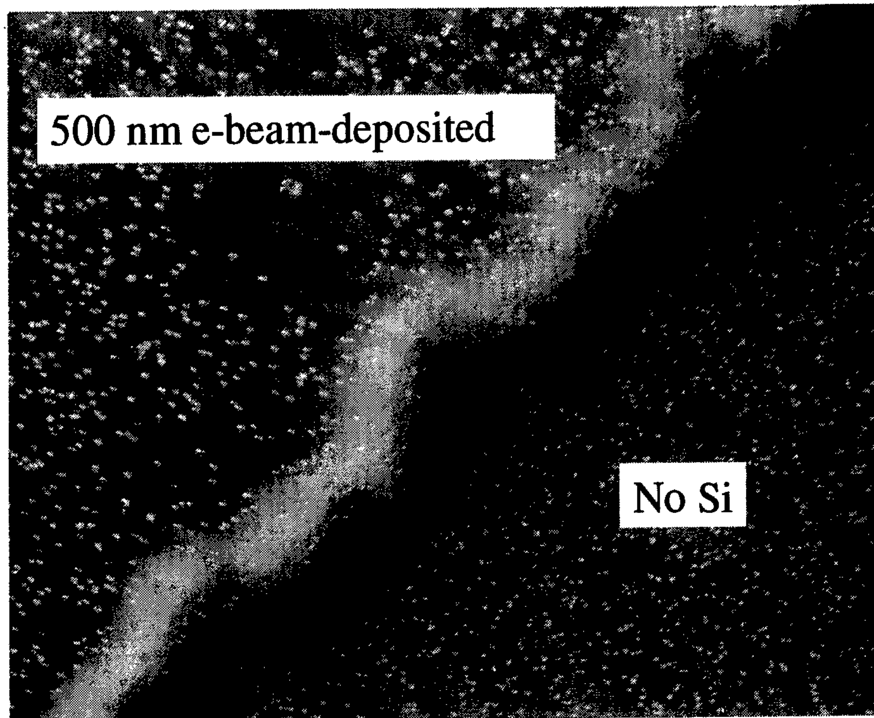

Figure 23. A photograph of wafer JGK-0090 partially coated with CVD-deposited Si. The vertical striations are an artifact of the computer-copying-pasting process.

This photograph shows the wafer covered with tiny defects that are 150-nm-high bumps. They are on the surface of the wafer. Later wafer growths eliminated this surface defect problem. The vertical striations are an artifact of the computer-copying-pasting process.

Amorphous Silicon (a-Si) Ridge Waveguides

To improve the Si waveguide, Sarnoff replaced e-beam deposited silicon with plasma-enhanced-chemical vapor deposited amorphous silicon (a-Si) [13]. The following is a review of a-Si as it applies to optical waveguides.

Since the invention of the amorphous silicon (a-Si) solar cell in 1976 at RCA/Sarnoff [14], the material has been extensively investigated for applications in large area electronics. The optical properties of a-Si (refractive index and optical absorption in visible and infrared regions) can be varied by alloying a-Si with germanium, carbon, or nitrogen. Amorphous silicon compounds can be easily doped p- or n-type with boron or phosphorous, respectively. Several companies have manufactured amorphous silicon solar panels larger than 1 m^2 in area and with conversion efficiencies > 8%. In their early years, active matrix liquid crystal displays all were manufactured using a-Si thin-film transistors.

While several methods are available to deposit a-Si films, plasma enhanced chemical vapor deposition (PECVD) is by far the most widely used technique for electronic device grade materials. PECVD is a proven technique for Si and III-V optoelectronic device processing as well, since it is used extensively for the deposition of inter-metal dielectric and passivation layers, such as silicon oxides and nitrides. Deposition of a-Si by PECVD is also expected to be fully compatible with III-V processing, since the deposition temperature is below 350°C,

and the material can be etched using fluorine-based plasmas, which offer good selectivity relative to InP.

Amorphous Si has a direct optical bandgap of about 1.7 eV. Figure 24 shows the optical absorption of a typical a-Si sample, compared with that of crystalline silicon (c-Si), as a function of photon energy. The sub-bandgap absorption coefficient (E_{ph} < 1eV) can be as low as 0.1 cm^{-1}, which is suitable for low-loss infrared waveguide applications.

The room-temperature conductivity of typical device-quality a-Si can be controlled from $\sim 10^{-10}\ \Omega^{-1}cm^{-1}$ to $\sim 10^{-4}\ \Omega^{-1}cm^{-1}$ p-type and $\sim 10^{-2}\ \Omega^{-1}cm^{-1}$ n-type by doping with boron and phosphorous, respectively. Heavy doping, however, results in a higher defect density and consequently an increase in the sub-bandgap optical loss.

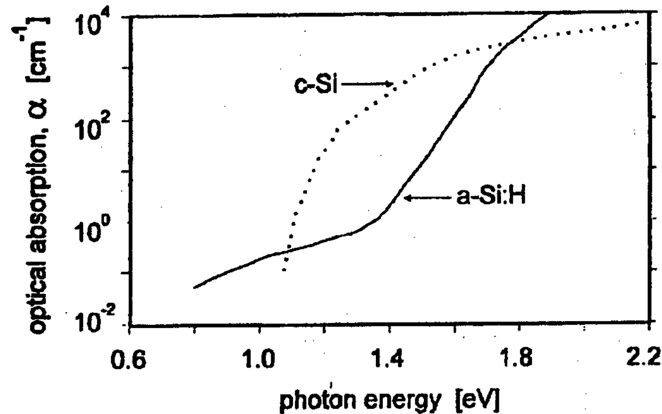

Figure 24. Optical absorption coefficient as a function of photon energy for a typical a-Si:H film made by plasma-enhanced chemical-vapor deposition. The sub-bandgap absorption was measured by photo-thermal deflection spectroscopy. The absorption coefficient of crystalline silicon is shown for comparison.

The refractive index of PECVD deposited films can be easily adjusted through alloying with a suitable choice of gases and flow ratios. The table below shows examples of how films with refractive indices ranging from 2.4 to 3.7 can be deposited in a single system. Over this entire range of refractive indices, it is possible to grow films with very low optical loss (< 0.1 cm^{-1}) for $\lambda > 1.3\ \mu m$. Several groups have successfully used PECVD silicon oxides and oxynitrides for waveguide applications. Silicon rich nitride and carbide films have been investigated as higher index waveguide materials with promising results [15].

Material	Gases	N/Si, C/Si ratio in film	Refractive index
Silicon-rich nitride	SiH_4, N_2	0.05-1.0	2.4-3.7
Silicon-rich carbide	SiH_4, CH_4	0-1.0	2.6-3.7

Figure 25(a) shows the refractive index as a function of N_2/SiH_4 flow ratio for a set of samples deposited at Sarnoff. Figure 25(b) shows the refractive index as a function of CH_4/SiH_4 flow ratio for a set of silicon carbide samples.

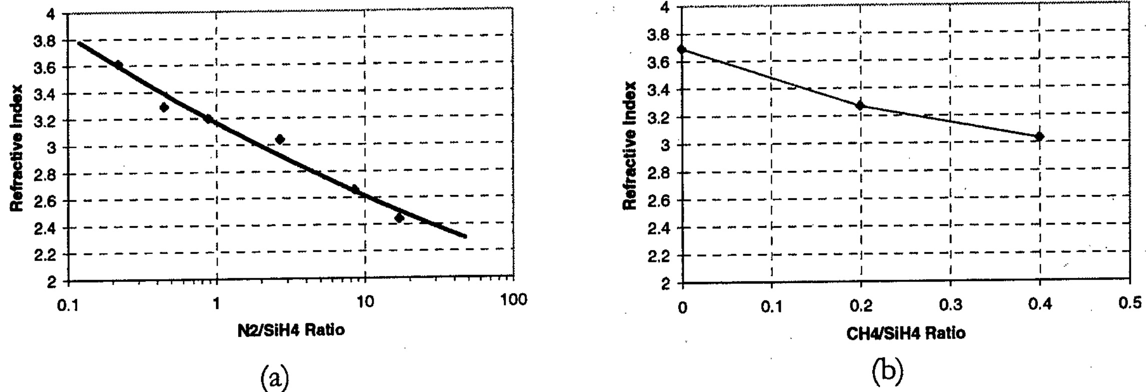

Figure 25. (a) Refractive indices of a series of a-SiN_x films made by varying N_2/SiH_4 ratio in the PECVD deposition; (b) refractive indices of a series of a-SiC for films using a gas mixture of SiH_4 + CH_4 + H_2.

Sarnoff has fabricated and demonstrated an a-Si nitride waveguide using SF_6 for plasma etching. Figure 26 shows the SEM picture of such a waveguide with relatively smooth etched sidewall surfaces. The high-quality, cleaved waveguide facet is also shown in Figure 26.

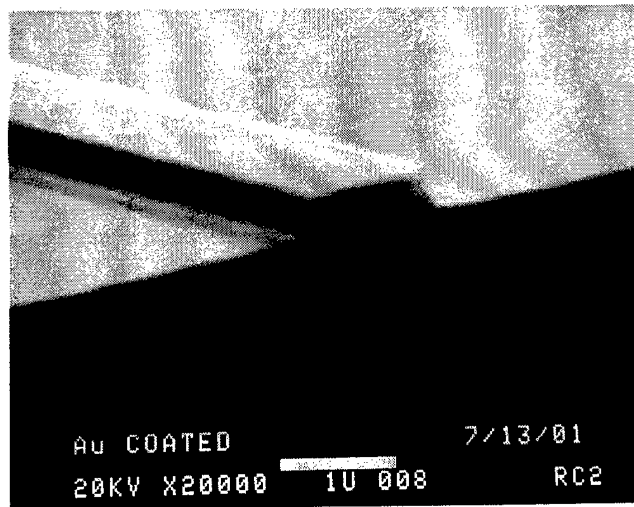

Figure 26. SEM picture of a cross section of an a-SiN_x ridge waveguide with n = 3.4 made on SiO_2 coated c-Si substrate. An SF_6 plasma was used to etch the waveguide.

Characterization of a-Si-Coated Optically Pumped 3.2-µm Lasers

Wafers JGK0116 and 00150 were coated with 0.8 µm of a-Si, which has a refractive index of 3.4. Both wafers have the same layer structure as shown in Figure 27.

Structure of JGK0116 and JGK0150 sample with a-Si waveguide								
Layer	Structure	Thickness (Å)	Repeats	Index				
Waveguide	a-Si	~8000	1	3.4				
Cap	GaSb	1000	1	3.73				
Hole Blocker	$AlAs_{0.08}Sb_{0.92}$	100	1	3.18				
					InAs	GaSb	InAs	AlSb
Active	InAs/GaSb/InAs/AlSb W	1080	10	3.49	20 Å	30 Å	20 Å	38 Å
					(confinement factor = 9%)			
Hole Blocker	$AlAs_{0.08}Sb_{0.92}$	100	1	3.18				
SCH	GaSb	4000	1	3.73				
Bottom Clad	$AlAs_{0.08}Sb_{0.92}$	20000	1	3.18				
Substrate	GaSb	0.5 mm		3.73				

Figure 27. Layer structure of wafers JGK0116 and JGK0150 coated after MBE growth with 0.8 μm of Si.

The wafers are identical, except that the growth temperatures of the ten W-QWs were different. The W-QW growth temperature, T_{QW}, for JGK0116 was 180°C below the GaSb substrate oxide desorption temperature, T_{ox}, and T_{QW} for JGK0150 was 200°C below T_{ox}. T_{QW} was decreased to clear up a surface defect problem that appeared on the surface of JGK0090 when T_{QW} was 130°C below T_{ox}. The density of surface defects decreased with lowered W-QW growth temperature: wafer JKG0150 had a much lower density of surface defects than did JGK0116. Recall that as discussed above, the surface of wafer JGK0090 was shown to have a very high density of surface defects (see Figure 23).

Portions of wafers JGK0116 and 0150 were sent to NRL for testing and characterization. They were cleaved into 2-mm-wide bars and optically pumped with pulsed 1064-nm radiation from a Nd:YAG laser. The beam was focused into a 150-μm-wide stripe parallel to the width of the bar. The bar facets were uncoated. These characterization experiments served to qualify the wafer for further processing, as we discuss below.

Figures 28 and 29 show the pulsed-mode output-power characteristics (L-L) of devices from wafers JGK0116 and JGK0150, each taken at four different temperatures from 78 to 150 K. (Henceforth, we refer to each as 116 and 150). The pump stripe widths are 150 μm. The cavity lengths are 2 mm. The 1.064-μm pump laser pulse width is 88 ns, and the repetition rate is 5 Hz for a duty cycle of 4.4×10^{-7}. Above threshold the L-L curves are linear. At 78 K the threshold power, P_{th}, is about 175 W/cm^2, and the maximum output power, P_{max}, is 100 mW. This threshold power density is 34 times lower than that found for lasers from JGK-0090. Both threshold power and output efficiency decrease with increasing temperature.

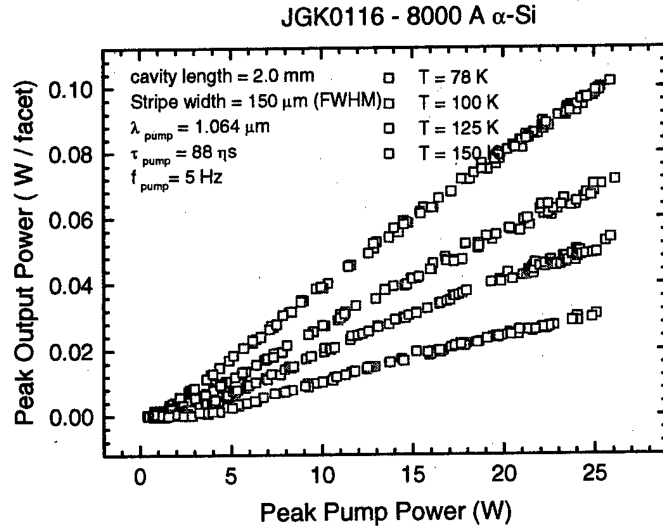

Figure 28. Output-power characteristics of an optically pumped laser from JGK0116 at four temperatures.

Figure 29 shows the pulsed-mode L-L curves for 0150, again at four different temperatures.

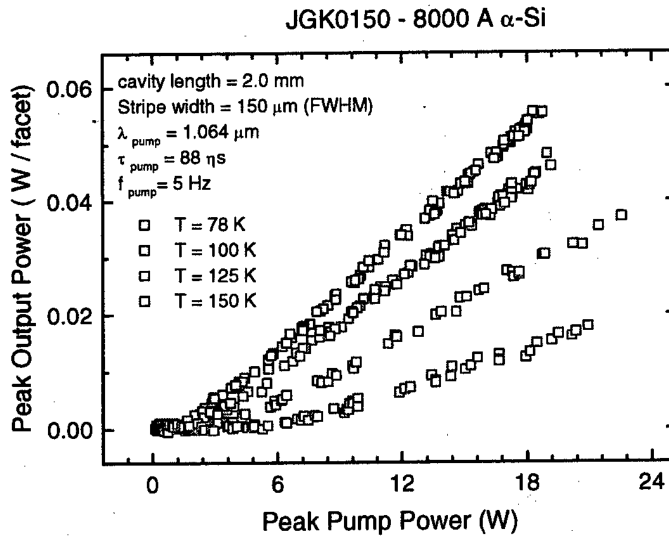

Figure 29. Output-power characteristics of an optically pumped laser from JGK0150 at four temperatures.

At 78 K, P_{th} is about 200 W/cm^2, a little larger than that of 116. At 18 W input power, the output power, P_{out}, is about 56 mW, whereas 116 outputs 75 mW for an 18-W input. Comparing the L-L curves for 116 and 150, the performance of 150 is poorer.

This difference in performance is seen in a closer look at the temperature variations of the operational parameters. Figures 30 and 31 show the increase of P_{th} with increasing temperature for 116 and 150.

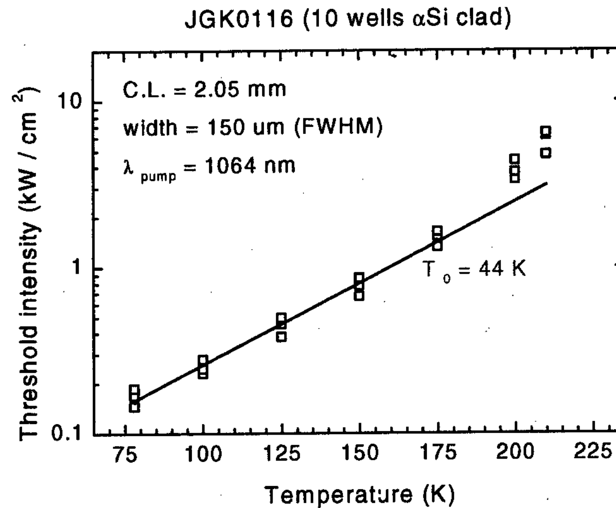

Figure 30. The exponential increase of the threshold power with increasing temperature for devices 116.

Between 78 and 175 K, the characteristic temperature, T_0, is 44 K. Above about 200 K, P_{th} increases rapidly.

T_0 for devices 150 is 39 K, which means that P_{th} for 150 rises more rapidly with increasing temperature than does 116. Above 200 K, P_{th} begins to run away with increasing temperature. For both 116 and 150, operation above 200 K was unstable, owing to the high input optical powers required to sustain lasing. T = 200 K is the maximum operating temperature for both lasers.

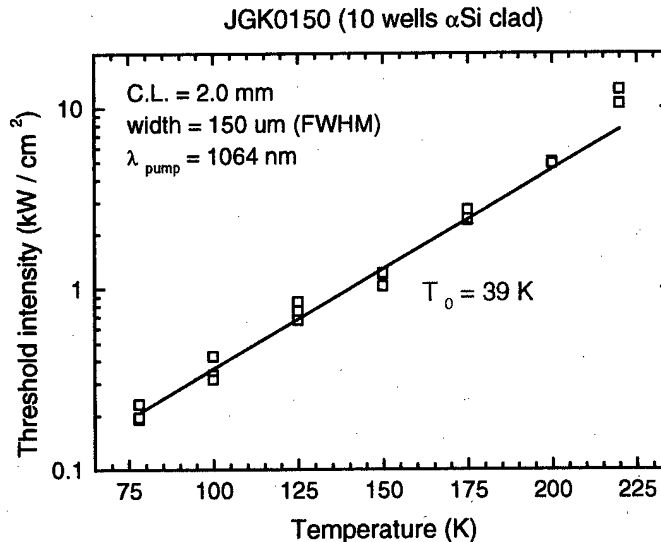

Figure 31. The exponential increase of the threshold power with increasing temperature for devices 150.

Figures 32 and 33 show the decrease of the external quantum efficiency, η_d, with increasing temperature for devices from 116 and 150, in dimensions of unit power output per facet per

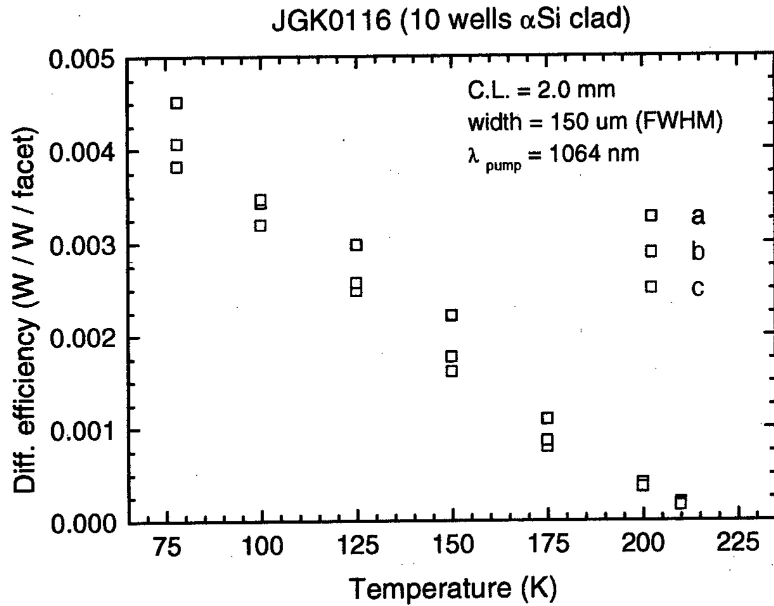

Figure 32. The decrease of the external efficiency with increasing temperature of 3 lasers from 116 unit incident pump power. Note that in terms of photons out per facet per incident pump photon, η_d = 0.012 at 78 K, which is threefold higher than the slope efficiency in W/W.

The data were taken from three regions along the bar: left, center and right. The exact points will be shown below. η_d = 0.0042 at 78 K, which is quite low, and it becomes nearly zero at 210 K.

Figure 33 shows η_d for 150. It is 0.0035 at 78 K, and it approaches zero at 200 K

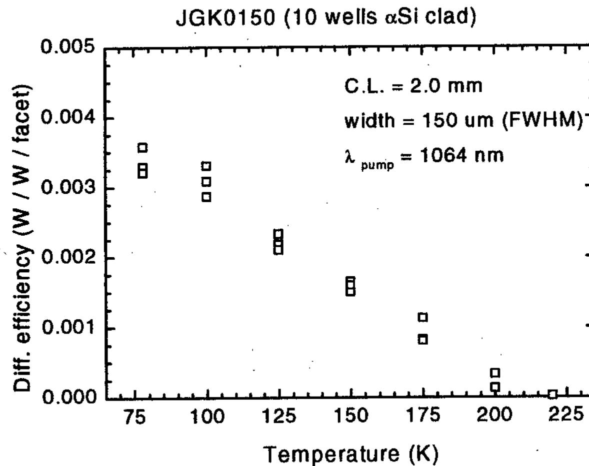

Figure 33. The decrease of the external efficiency with increasing temperature of 3 lasers from 150.

Figures 30 to 33 show that 116 has better output characteristics than does 150. Most likely, the lower growth temperature of the W-QWs in 150 produced poorer quality material.

The uniformity of the laser bars is exhibited in Figures 34 and 35. An approximately 1-cm-long bar is pumped as a 2-mm-long laser along its width. The 150-μm-wide pump stripe is moved 0.5 mm along the bar. Points a, b, and c are indicated. The efficiency varies slightly along the bar, tending to decrease somewhat going from left to right. The maximum value of η_d is 0.005 at point a. The uniformity of η_d for lasers along the bar is reasonably good.

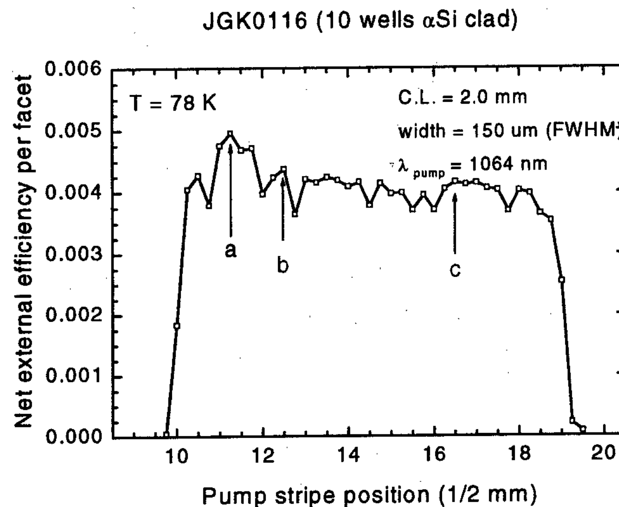

Figure 34. The external efficiency at 78 K for lasers at 0.5-mm intervals along the bar from JGK0116.

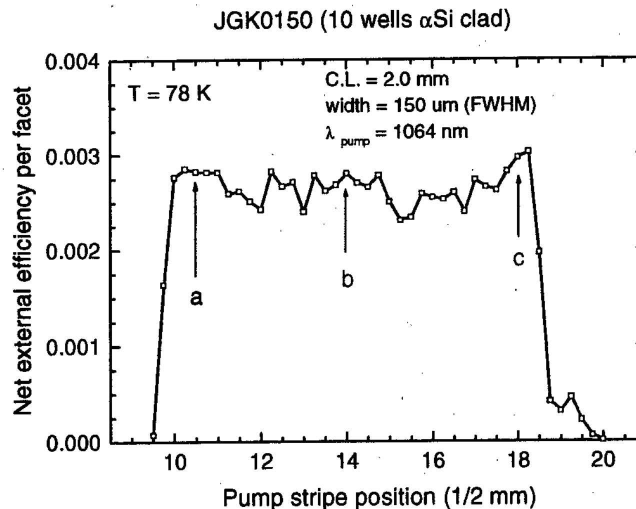

Figure 35. The external efficiency at 78 K for lasers at 0.5-mm intervals along the bar from 150.

Lasers from 150 also exhibited reasonably good uniformity of η_d, but as noted above the maximum value of η_d is about 40% lower at 0.003.

Output spectra for lasers from 116 and 150 are shown in Figures 36 and 37.

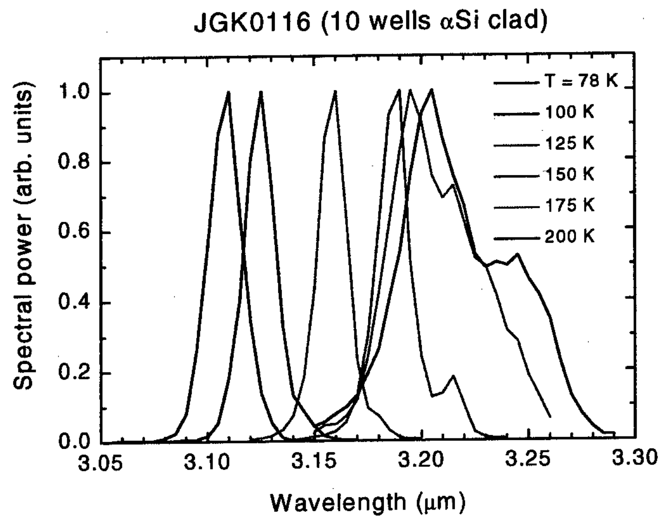

Figure 36. The output spectra of a laser from 116 at six different temperatures.

From 78 to 150 K the spectra are single-lobed. Above 175 K the spectra broaden significantly. Note well that the resolution of the spectrometer with which these spectra were taken is only 5 nm, so the "single-lobed" spectra actually contain many unresolved modes of the laser. The broadening of the spectra indicates the presence of amplified spontaneous emission, near the maximum temperature of lasing operation. The device begins to act as a light-emitting diode with a small optical gain. Whereas the narrowing of the output spectrum indicates the onset of laser action, the subsequent broadening indicates the cessation of laser action.

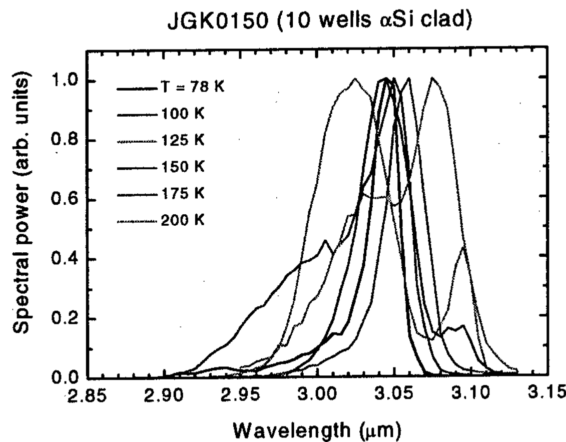

Figure 37. The output spectra of a laser from 150 at six different temperatures.

The spectra of lasers from 150 are more irregular than those of laser 116, as seen in Figure 37. There is no uniform increase of the wavelength with increasing temperature, and spectral broadening begins at 100 K.

Figure 38 shows the temperature dependence of the wavelength of lasers from 116. Between 78 and 150 K, the wavelength of the central peak of the spectra increases at the rate of 1.12 nm/K, which is typical for antimonide-based mid-infrared lasers.

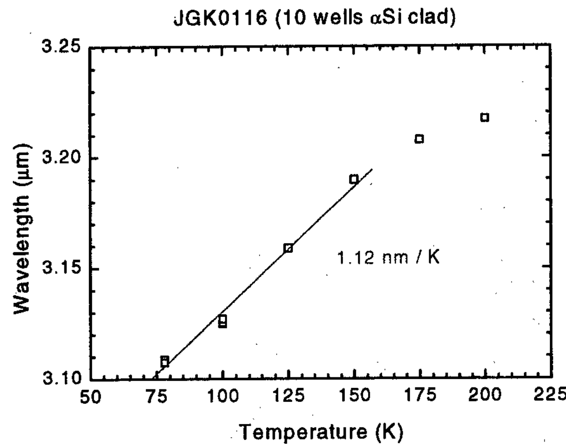

Figure 38. The temperature dependence of the wavelength of lasers from 116.

The data presented suggests that 116 performs better than 150. The low external efficiency of 150 implies that the lower growth temperature of the QWs produces QWs of inferior optical gain. Subsequent devices were grown as 116 was grown.

The low efficiency of 116, and hence the low maximum operating temperature of 200 K, may be due, in part, to the fact that the pump wavelength was 1064 nm, which is absorbed by the GaSb layers within the device (see Figure 27).

MBE Growth and Characterization of Additional Sarnoff SOAs

Room temperature photo-pumped lasing experiment on gain-guided samples of JGK0116 and JGK0150 demonstrated that these structures lase at 3.5 μm. In order to adjust the center wavelength of the laser structure to be at 3.25 μm, a new W-QW structure (JGK0234), as shown in Figure 39, was designed and grown.

Structure of JGK-0234								
Layer	**Structure**	**Thickness (nm)**	**Repeats**	**Index (3.25 um)**				
Cap	GaSb	10	1	3.73				
Hole Blocker	$AlAs_{0.08}Sb_{0.92}$	10	1	3.18				
					InAs	GaSb	InAs	AlSb
Active W-QW	InAs/GaSb/InAs/AlSb W	196	20	3.49	17.5 Å	30 Å	17.5 Å	33 Å
Hole Blocker	$AlAs_{0.08}Sb_{0.92}$	10	1	3.18				
SCH	$Al_{0.5}Ga_{0.5}As_{0.04}Sb_{0.96}$	800	1	3.73				
Bottom Clad	$AlAs_{0.08}Sb_{0.92}$	2000	1	3.18				
Buffer	GaSb	500	1	3.73				
Substrate	GaSb	Thick		3.73				

Figure 39. The layer structure of an optically pumped 3.25-μm W-QW laser (JGK0234).

After growing a 500-nm-thick GaSb buffer layer, a 2-µm-thick $AlAs_{0.08}Sb_{0.92}$ bottom-cladding layer was grown, followed by the growth of a 800-nm-thick $Al_{0.5}Ga_{0.5}As_{0.04}Sb_{0.96}$ separate-confinement-heterostructure (SCH) layer. Next, an $AlAs_{0.08}Sb_{0.92}$ hole-blocking layer was grown. This layer helps to confine holes in the active region.

The active region comprising 20 W-QWs is grown. Each well is an InAs(1.75nm)/GaSb(3nm)/InAs(1.75nm) type-II W-QW that is calculated to lase at 3.25 µm at room temperature. A 3.3-nm-thick AlSb barrier surrounds each well, except the first one, which has a 10-nm-thick $AlAs_{0.08}Sb_{0.92}$ barrier. The PL and lasing wavelength of the W-QWs is determined by the InAs thickness.

The structure is completed by growing 10-nm-thick hole-blocker layer, on top of which is grown a 10-nm-thick GaSb layer that inhibits oxidation of the Al.

Wafers JGK0234 and JGK0150 were then coated with 800-nm of PECVD-deposited Si, and they were processed as ridge-waveguide (RWG) lasers. The results for RWG lasers will are reported below.

In addition to the a-Si-coated structure, a GaSb waveguide structure (previously grown by G. Turner at MIT-LL) was duplicated at Sarnoff MBE reactor (JGK0244) as shown in Figure 40. This structure was processed separately at Sarnoff.

Layer	Structure	Thickness (Å)	Repeats	Index				
Top waveguide	GaSb	5000	1	3.73				
Hole Blocker	$AlAs_{0.08}Sb_{0.92}$	100	1	3.18				
					InAs	GaSb	InAs	AlSb
Active	InAs/GaSb/InAs/AlSb W	1960	20	3.49	17.5 Å	30 Å	17.5 Å	33 Å
Bottom Clad	$AlAs_{0.08}Sb_{0.92}$	20000	1	3.18				
Substrate	GaSb	Thick		3.73				
	Total MBE Thickness (µm)	2.706						

Figure 40. The structure of GaSb-waveguide 3.25-µm W-QW laser.

Description of a-Si Ridge Waveguide Processing

Figure 41 shows schematically the a-Si RWG fabricated on laser wafer JGK0150.

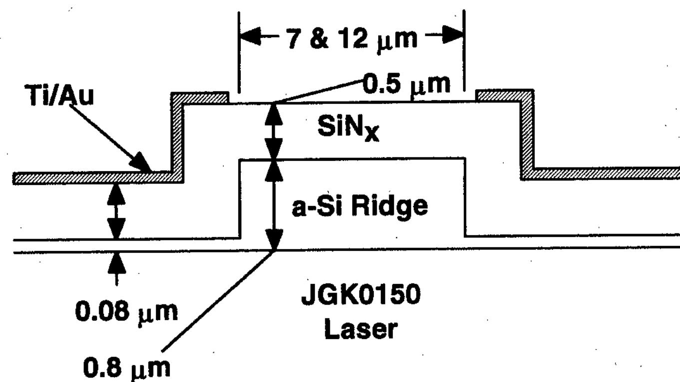

Figure 41. Schematic diagram of the a-Si ridge waveguide.

The top surface of the wafer was coated with 0.8 μm of a-Si, which had a measured refractive index of 3.4. Using a DE101 plasma, ridge waveguides were etched into the a-Si, leaving about 0.08 μm of a-Si. (DE101 is 98% He, 1.6% CF_4, and 0.4% O_2.) The ridge widths were 7 and 12 μm. Three types of waveguides were made: straight waveguides normal to the laser facets, straight waveguides slanted at an angle of 6°, and curved waveguides normal to the output facet of the ECL and at 6° to the laser facet that is interior to the ECL (see Figure 13). The ridges were conformally coated with 0.5 μm of SiN_x. Ti(10 nm)/Au(100 nm) was then deposited at ambient temperature everywhere, except on the ridges. The metal acts as an optical mask, so that only the laser active region beneath the ridge is optically pumped. This prevents the formation of Fabry-Perot lasers outside the RWG.

An error occurred during processing, and the metal was misaligned over the ridge, resulting in part of the ridge being obscured. Figure 42 shows scanning electron microscope photographs depicting the situation.

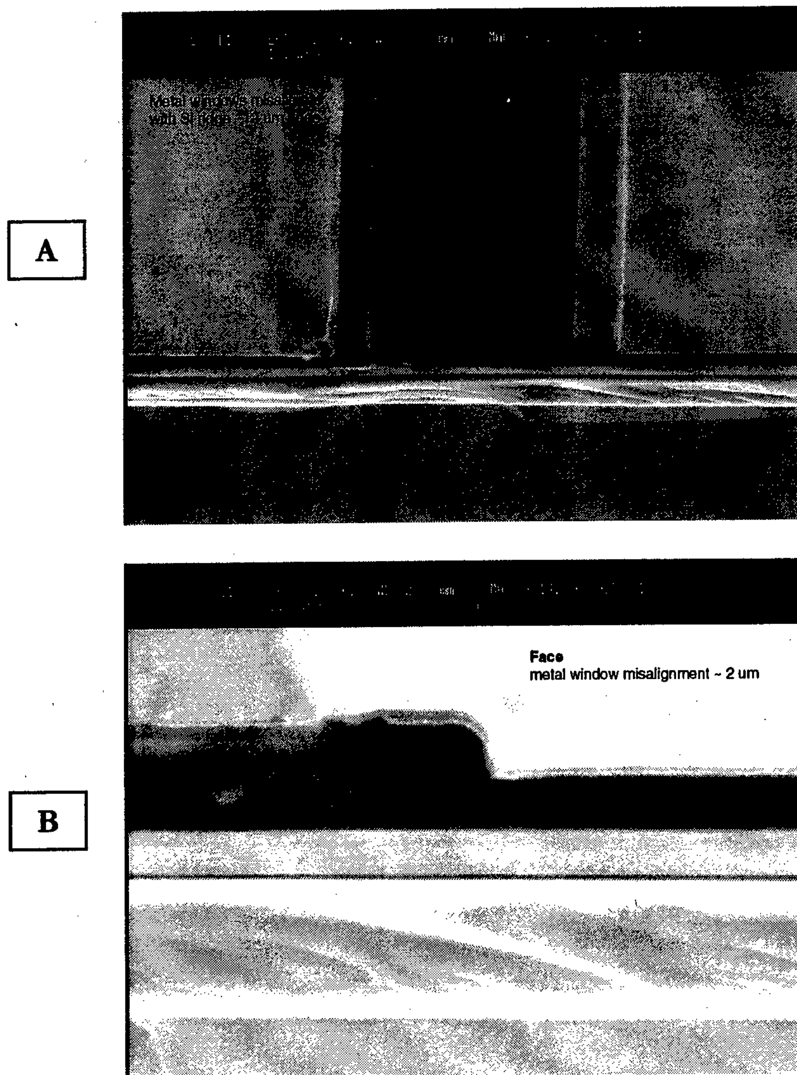

Figure 42. SEM images of metal 2-μm overlap of a-Si ridge waveguide.

The metal mask overlaps the RWG by about 2 μm, as shown clearly in Figure 42-B. This means that a fraction of the active region beneath the RWG is not pumped. The metal may also create optical loss for the fundamental mode that is guided by the RWG.

In subsequent fabrications a 5-μm gap on each side of the RWG was to be allowed. This makes photo-mask alignment during device processing much easier. With such a gap the metal should still act as a mask to inhibit Fabry-Perot laser action outside the RWG.

Laser Results on a-Si Straight/Normal Ridge Waveguides

Despite the misalignment of the metal, bars of RWG lasers were cleaved and facet-coated. The facet where all RWGs are normal to it was coated to reflect 90% at 3.2 μm, and the opposite facet was coated to reflect 4%. The cavity length (or bar width) was 1.5 mm. The straight/normal RWG were optically pumped with 2-μm radiation in the pulsed mode (100 ns, 4 kHz). The 2-μm pump radiation is more strongly absorbed and has a smaller quantum defect than a 1-μm radiation.

Figure 43 shows the output-power characteristics of the laser at T = 295 K.

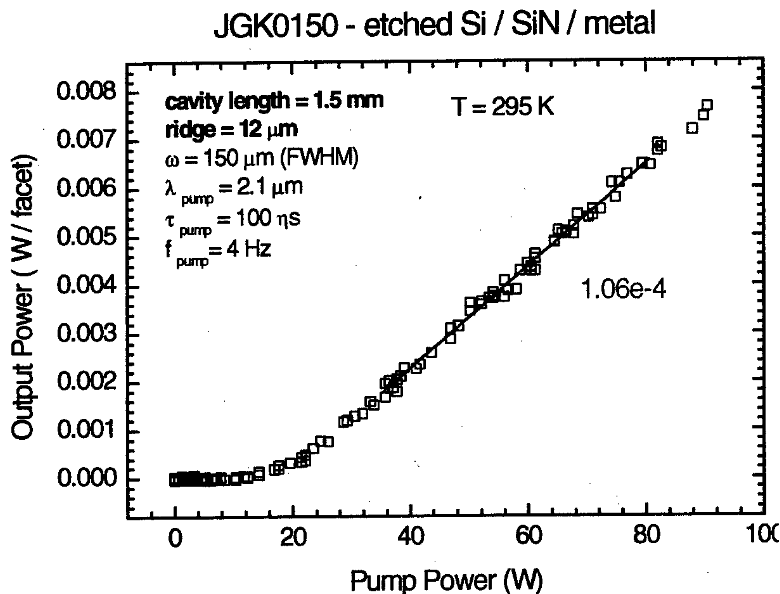

Figure 43. Output-power characteristics for an optically pumped straight/normal a-Si RWG on laser wafer JGK0150 at a temperature of 295 K.

In this case the RWG is 12-μm wide. The pump laser stripe width, ω, is 150 μm (FWHM). The threshold power is about 18 W (100 kW/cm^2). The slope efficiency, measured as power out per facet divided by pump power in is about 0.01%. This is a very low value; about 3% is expected [12]. Note, however, that the operating temperature is 295 K.

One sixth of the 12-μm RWG and about one third of the 7-μm RWG is masked by the metal, and 2 μm outside the RWG is pumped, so the RWG is non-uniformly pumped. This greatly distorts the mode structure. The metal overlap may also induce optical losses.

Figure 44 shows the threshold pump power as a function of temperature for 7- and 12-μm-wide RWGs and also for an optically pumped laser from wafer JGK0150 with an a-Si top layer, but without an etched RWG. All cavity lengths are 1.5 mm.

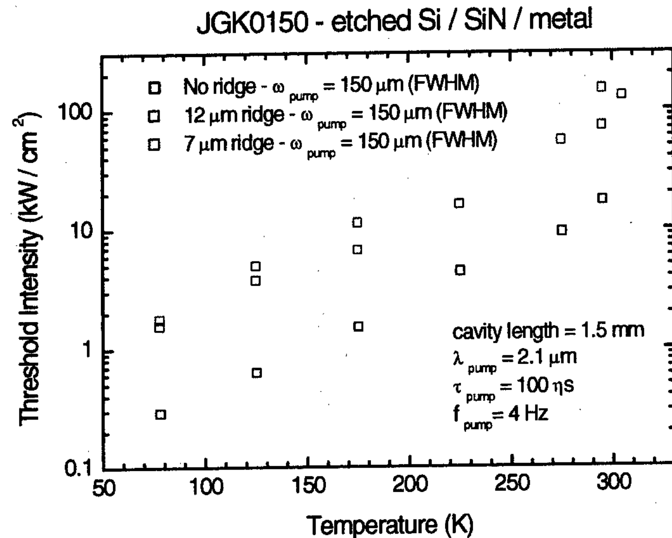

Figure 44. The temperature dependence of the threshold current for RWG *and non-*RWG *lasers from wafer JGK0150.*

The threshold power, P_{th}, for all three lasers increases exponentially; that is, P_{th} is proportional to $\exp(T/T_0)$. The characteristic temperature, T_0, for all the devices is about 54 K. The fact that P_{th} for the non-RWG laser is about 10 times lower than those of the RWG lasers may be the result of higher intrinsic losses in the RWG itself coupled with losses due to metal misalignment. The 12- and 7-μm RWGs have about the same P_{th} at all temperatures. All devices operate at room temperature.

Figure 45 shows the lateral far-field pattern for the 7-μm RWG laser at T = 295 K.

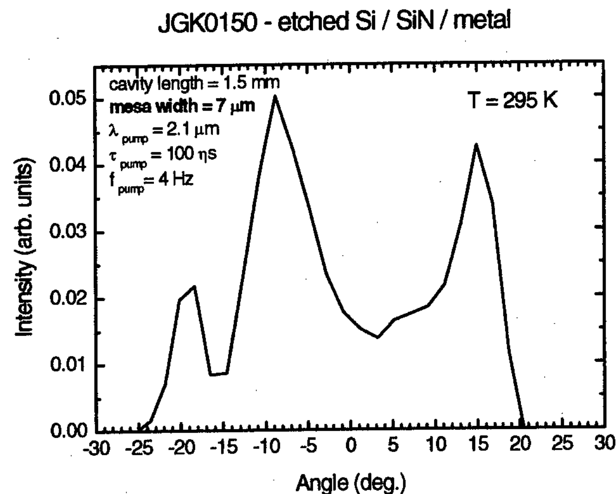

Figure 45. Lateral far-field pattern for a 7-μm-wide a-Si RWG *on wafer JGK0150.*

The pattern is multi-modal and unsymmetrical. From simple diffraction theory, the half angle at which the far-field pattern of a uniformly illuminated aperture of width d first reaches zero intensity is λ/d, in which λ is the wavelength. In our case $\lambda/d = 3.25/7$ is about

26°, which is approximately true for the data in Figure 44. The fact that the far-field pattern is multimode casts doubt on the relevance of using such a simple model.

Figure 46 shows the far-field pattern from an optically pumped 12-μm-wide RWG.

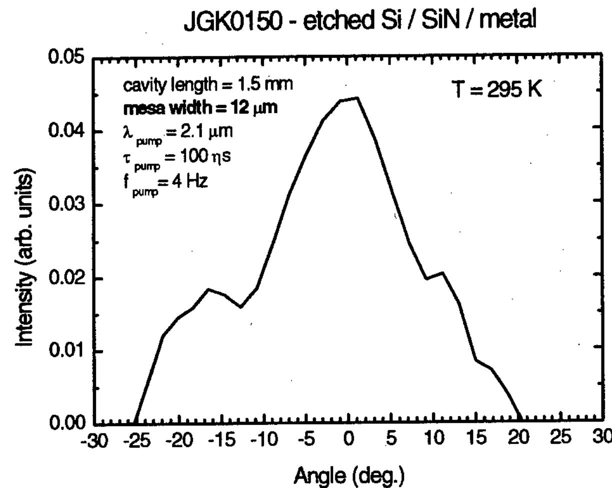

Figure 46. Lateral far-field pattern for a 12-μm-wide a-Si RWG on wafer JGK0150

The pattern is less distorted than that of the 7-μm-wide RWG laser (see Figure 45). The diffraction angle is similar. It may be that the overlaping metal governs the shape of the near-field mode in both cases.

SOA Summary and Conclusions

We developed optically pumped, amorphous silicon ridge-waveguide lasers that could be used as curved ridge waveguide semiconductor optical amplifiers. This was done through the parallel effort of growing an optimal laser structure via molecular-beam epitaxy and through optimizing a ridge-waveguide design. The resulting lasers operated up to a temperature of 295 K with no sign of output power saturation or of a runaway in the threshold current. At 295 K they output 7 mW per facet. Comparison with a stripe laser in the same material suggested that flaw in the placement of the ridge metal mask induced losses that increased the threshold pump power by an order of magnitude. The flaw was an overlap of the metal onto the ridge that masked off pump light. The wavelength of this laser varied from 3.05 μm at 78 K to about 3.10 μm at 295 K. The lateral far field patterns for both 7-μm-wide and 12-μm-wide ridge-waveguide lasers were multi-lobed, indicating that the lasers were not operating in the fundamental lateral mode.

We had SOA designs using GaSb ridge-waveguides etched into the grown laser structure. These were midway through processing when the project ended.

The successful operation of the 3-um optically pumped ridge waveguide laser is partially due to the redesign of the ridge. This redesign placed a silicon-nitride layer between the metal mask and the antimonide cladding layer of the laser. In this way any optical losses caused by the metal were reduced. This approach should produce efficient SOAs for the external cavity laser. The inadvertent overlap of the metal onto the ridge may have caused the low external efficiency, and hence, low output power of the laser.

IV. External Cavity Calculations and Experiments

The External Cavity Laser: General Considerations

The design and analysis of the external cavity (EC) is given below. A simpler Littrow configuration is also included.

As a guide to the configuration, Figure 47 shows a schematic of the external-cavity laser.

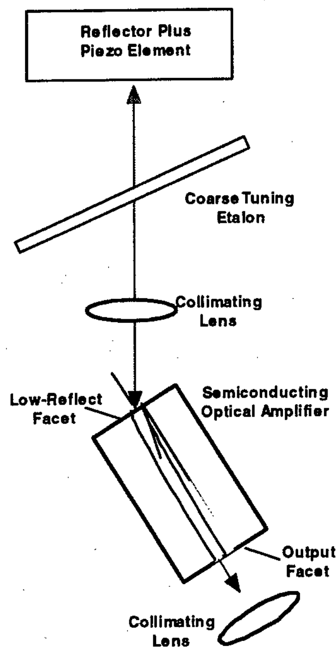

Figure 47. The essential elements of the tunable external cavity laser.

A high-Finesse etalon is used as the coarse tuning element within the external-cavity laser. An analysis of the optical requirements placed on the tuning etalon is presented, based on single-mode selection.

There are two constraints placed on the etalon, determining the linewidth and free-spectral range (FSR) that ensure selection of a single longitudinal mode of the EC. First, the etalon transmission peak must be sufficiently narrow to select a single longitudinal mode that excludes adjacent EC modes. Further, the subsequent etalon transmission peaks must occur outside the gain spectrum to prevent additional etalon orders from overlapping with relevant cavity modes. Figure 48 shows the EC mode spectra of the EC modes, the tuning etalon, and the SOA gain spectrum.

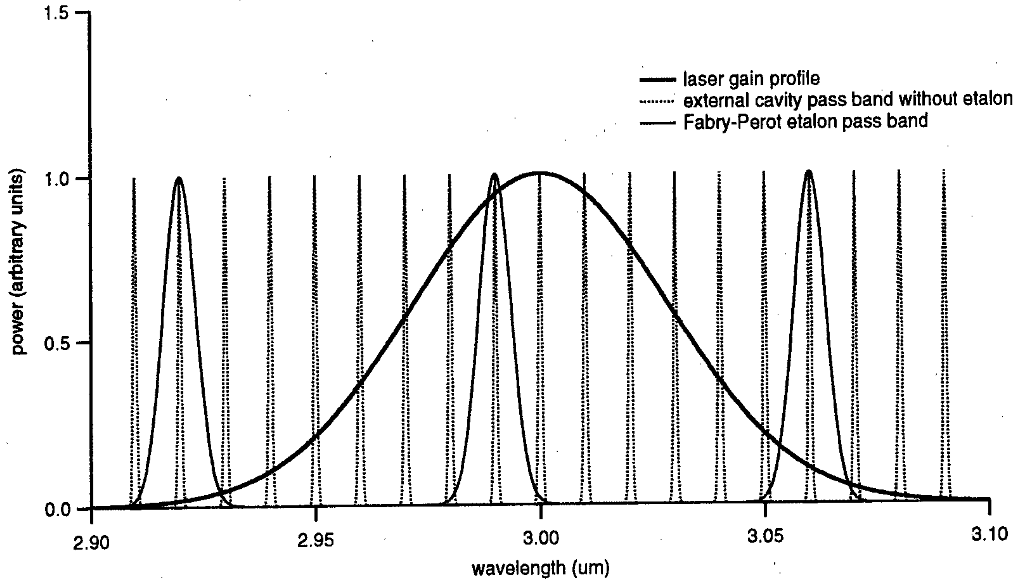

Figure 48. The schematic mode spectra of the external cavity and the coarse-tuning etalon, along with the gain spectrum of the semiconductor optical amplifier

In actuality, the free spectral range of the tuning etalon need not be an integral multiple of the EC mode spacing, as shown in Figure 48.

To begin this analysis, note that the cavity mode spacing is determined by $\nu_c = c/2nL_c$, where c is the speed of light in vacuum, n is the group velocity index, and L_c is the cavity length. To prevent adjacent cavity modes (red curves) from lying beneath the etalon transmission profile (blue curves), the etalon transmission linewidth, $\Delta\nu_{res}$, should be less than the cavity mode spacing. So one can take $\Delta\nu_{res} = \nu_c/2$. Further, to have a single etalon transmission peak within the gain bandwidth, $\Delta\nu_{gain}$, the etalon free spectral range, ν_{FSR}, needs to span the gain bandwidth (**black** curve). Therefore, $\nu_{FSR} = \Delta\nu_{gain}$. We assume that the gain-bandwidth equals 10% of the optical frequency. That is, $\Delta\nu_{gain} = 0.1\ c/\lambda$, where λ is the laser free-space wavelength, which in our case is 3.2 µm. ν_{FSR} is, therefore about 9 THz. With these constraints, the etalon Finesse, and hence, the required optical reflectivity of the surfaces of the etalon, can be determined. The etalon Finesse is defined as $F = \nu_{FSR}/\ \Delta\nu_{res}$, and assuming that the reflective surfaces, R, making up the etalon are identical, $F = \pi R^{1/2}/(1-R)$. Based on these constraints, Figure 49 shows the needed etalon Finesse as a function of cavity length. The larger the cavity, the more finely spaced the external-cavity modes the higher the etalon Finesse must be to envelop a single longitudinal mode.

Figure 50 displays the reflectivity needed on each surface of the etalon to achieve the Finesse given in Figure 49. Reflective coatings greater than 99.8% are needed with bandwidths which span the region of interest.

The free-spectral range is determined by the etalon thickness, L_e. For example, a 6.6 µm thick ZnSe substrate (n = 2.4) or a 9-µm-thick Sapphire plate (n = 1.76) provides the needed free-spectral range of 9 THz ($\nu_{FSR} = c/(2nL_e)$). It is difficult to obtain plates of this thickness while maintaining good optical quality ($\lambda/10$ surface quality). On the other hand, an air-gap etalon comprising two parallel, highly reflective, optically flat plates that are

separated by a narrow gap can be assembled (see Figure 51). The back sides of each plate must be anti-reflection coated, or a wedged-plate can be used to prevent unwanted intra-cavity reflections. For an air-gap etalon, a gap spacing of 16 μm provides the required free-spectral range. Whether a solid or an air-gap etalon is used, losses due to scattering from imperfections or impurities on the etalon surface lead to a reduction in the Finesse, and optical performance suffers. It may be necessary to seal the etalon hermetically to avoid exposure to atmospheric contaminants that can increase scattering losses.

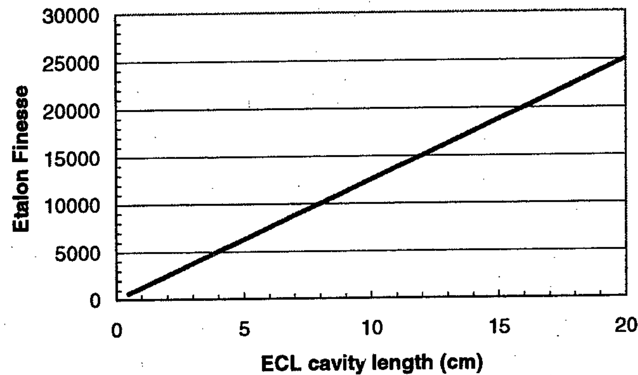

Figure 49. Etalon finesse needed to select a single longitudinal cavity mode. Etalon free spectral range is chosen to be 320 nm (9.4 THz), or equal to a gain-bandwidth of 10% of the optical frequency, which corresponds to a wavelength of 3.2 μm.

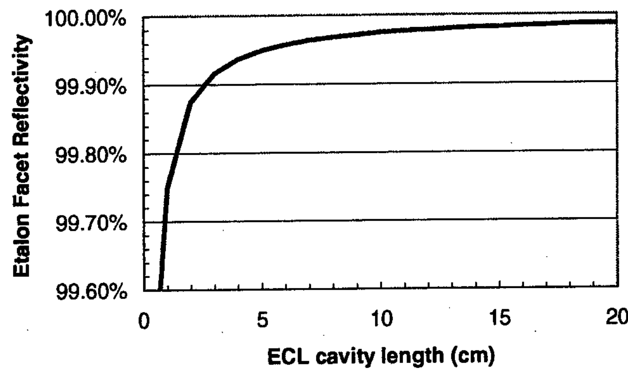

Figure 50. Corresponding mirror reflectivity needed to achieve etalon Finesse shown in Figure 49.

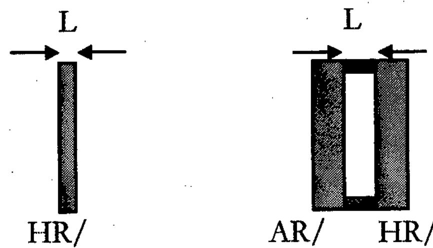

Figure 51. Schematic of solid (left) and air-gap (right) etalon. A ring spacer, such as ultra-low-expansion quartz, is used to set air-gap spacing.

The tuning characteristics of the etalon can be determined through a rotation from normal incidence. The rotation increases the etalon path-length, L_e; thus, changing ν_{FSR}. The important etalon transmission peak is the one that occurs at the wavelength range of interest, $N\nu_{FSR} = \nu_o$; where N is the order of the etalon and ν_o is the SOA center frequency. From the above conditions, N = 10 ($\nu_{FSR} = 0.1\nu_o$). For a full tuning range, it is necessary to increase the etalon path-length such that $N\nu'_{FSR} = \nu_{FSR}(N+1)$; where ν'_{FSR} is the new etalon free-spectral range after rotation. In other words, to cover the full tuning range, it is necessary to rotate the etalon so the transmission peak sweeps out one free-spectral range. Figure 52 shows the needed angular rotation of an air-gap etalon to allow tuning over one free-spectral range. The air-gap etalon is formed between two HR coated ZnSe substrates and a 10-degree rotation will provide the needed tuning range.

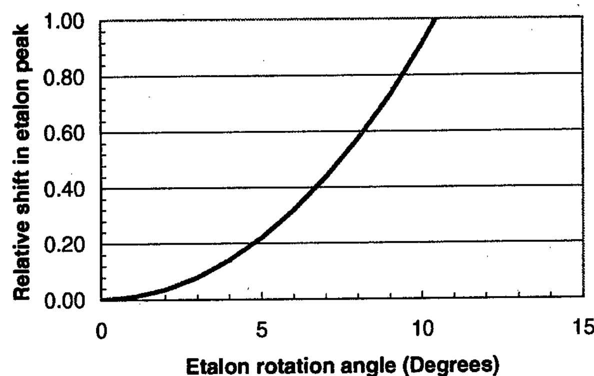

Figure 52. Wavelength tuning by etalon rotation. At ten-degrees rotation (off normal), the etalon transmission peak sweeps through one free-spectral range. The etalon is formed by a 16 μm air-gap between two HR/AR-coated ZnSe plates. The total external-cavity length has to be adjusted to maintain fixed cavity modes as etalon is rotated. Mounting the cavity end-mirror on a piezo actuator provides the needed length control, a total displacement of 1.6 μm (i.e. $\lambda_0/2$).

We located vendors to supply such an etalon. The company named II-VI, Inc. may have been able to provide the needed AR/HR coated ZnSe substrates, and a company such as Wave Precision may have been able to construct the air-gap etalon module. Owing to budgetary and time constraints, however, Sarnoff designed, fabricated and tested air-gap etalons.

Our preliminary design is based on the device gain peak wavelength of 3.75 μm and ECL tunable range of 200 nm. For the convenience of bench top operation, the cavity length is 8 cm. With this cavity length, the ECL cavity should support about 10^4 longitudinal modes, which is reasonable for most lasers. A coarse-tuning etalon selects a cavity mode and provides wavelength tuning. The etalon mode spacing is set to be the same as the ECL tunable range, namely 200 nm. The etalon linewidth is set to be half the ELC cavity mode spacing.

The 8-cm cavity length leads to the cavity-mode spacing of 1.88 GHz. The etalon thickness is determined by the 3.75-μm peak wavelength and tunable range of about 200 nm. We originally proposed a ZnSe-based solid etalon with its rotation to reach ECL tuning.

However, we learned from vendors that they have engineering difficulties fabricating the etalon with a thickness of 14.5 μm. Therefore, we changed our design to an air-gap etalon with two high reflection coated ZnSe mirrors. The gap width will be 16 μm, which corresponds to the etalon mode spacing of 9.5 x 10^3 GHz. This means that there are about 5,000 cavity modes between the two adjacent etalon modes. The etalon scan range is about 2 μm to cover the 200 nm bandwidth. In order to reach 1.8 GHz linewidth, the etalon needs to have a finesse of about 3,000, which implies an etalon mirror reflectivity of 99.9%. Figure 53 shows the relationship between etalon finesse and mirror reflectivity. While 99.5% reflectivity can be guaranteed, most vendors can only promise best effort for 99.9%.

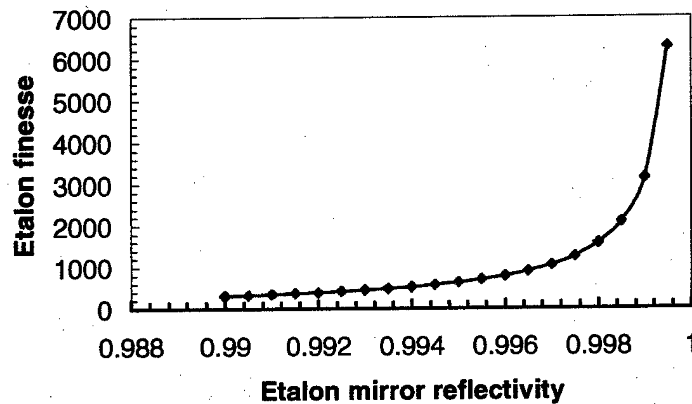

Figure 53. Etalon finesse increases with mirror reflectivity

While the etalon is tuned from 3.65 to 3.85 μm, the cavity length needs to be increased by about 4 mm, so a fixed cavity mode is always selected while the etalon is being tuned. Since typical piezo actuators only cover a range up to several hundred micrometers, we will need to couple a micrometer to the piezo to facilitate such a wide range cavity tuning.

The above design served as a guide for the required optical parts needed for the project.

Diffraction Grating as a Tuning Etalon

Use of a grating at the Littrow angle can also provide intracavity wavelength selection in a simpler optical configuration, with the caveat that multiple neighboring cavity modes may lase simultaneously (see Figure 54 for a Littrow configuration schematic). Despite this possible limitation, this configuration was pursued because of the relative ease in obtaining the gratings. This allows us to demonstrate proof-of-principle operation of a tunable external-cavity laser at the 3.2-μm wavelength.

To determine the Littrow condition, the grating equation is used under the condition that the diffracted angle, θ_L, is equal to the incident angle. Hence, $\theta_L = \lambda/(2d)$; d being the grating groove density. Figure 55 shows the Littrow angles as a function of d for a variety of center wavelengths.

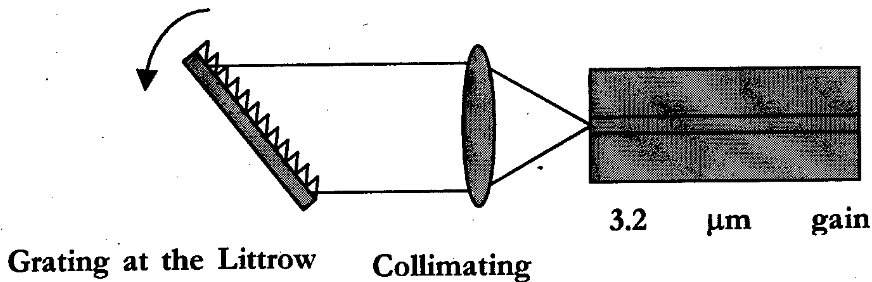

Figure 54. Schematic of grating-tuned external cavity laser. Under the Littrow configuration and for a given wavelength, the angle of diffraction equals the angle of incidence.

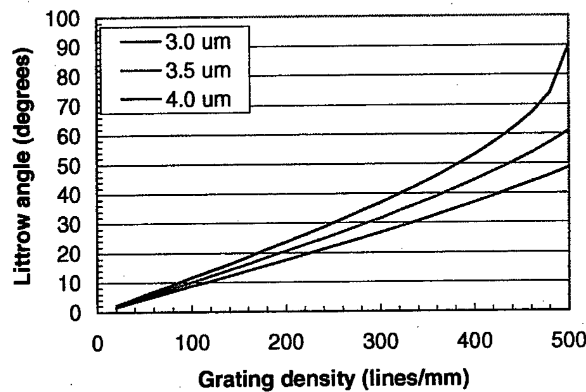

Figure 55. Littrow angles, θ_L, as a function of grating groove density for a variety of center wavelengths.

Spectragon, Inc. has master gratings in stock with groove densities of 300 and 500 lines/mm.

Tuning Etalon Design

As discussed above, a high-Finesse etalon is used as the tuning element within the external cavity laser. The etalon selects one of the longitudinal lasing modes of the gain medium. The design requires an optical thickness of nL_e = 16 µm, where n is the index of refraction, and L_e is the etalon cavity length. Sixteen microns is an awkward thickness that lies between the fabrication realms of epitaxy/deposition and mechanical manufacture. It has proven too difficult to find a good material for a solid etalon of this thickness. Materials that can be deposited on a flat substrate at this thickness have absorption losses too high for an etalon, in addition to there being issues of thickness uniformity.

An alternative is an air-gap etalon. Air losses are minimal. Scattering losses at interfaces must still be addressed. A design based upon a sandwich of two silicon wafers has been developed. Several materials including zinc-selenide, germanium, and others are transparent and very low loss over the operating wavelength of the laser. Silicon was chosen because of its flatness, material quality, established optical polishing techniques, and low cost.

Figure 56 shows the etalon fabrication process. Two silicon wafers will be polished into wedges and coated with a high-reflection (HR) coating on one side and an anti-reflection (AR) coating on the other.

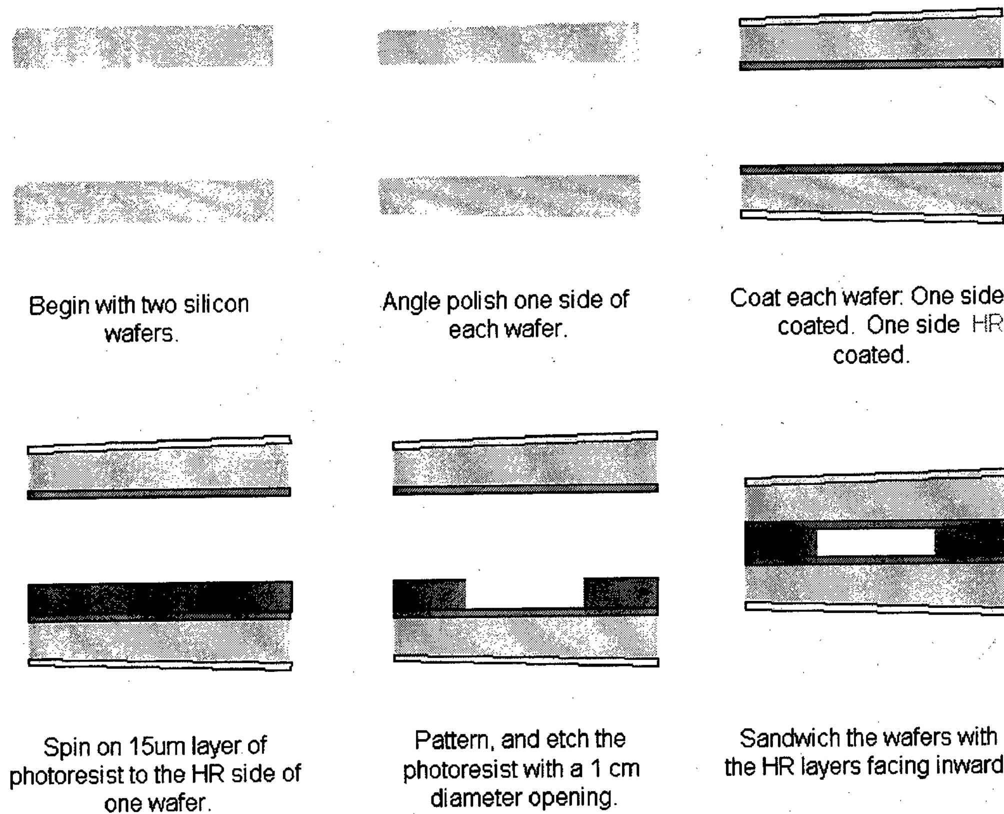

Figure 56. Tuning etalon fabrication process.

The AR coating and wedge prevents additional undesirable intracavity etalon effects. One of the wafers will be coated with a 15.5-μm-thick spin-on photoresist. One-centimeter diameter holes are patterned and etched in the resist. Both wafers are diced into a more manageable size (e. g., 1-inch squares). The bare and resist-coated wafers are sandwiched and held together to form the etalon.

The etalon requires both AR and HR coatings. The AR coatings cut down the reflection from the outer surfaces in order to eliminate the formation of multiple etalons. The wedge design reduces the performance demanded of the AR coating as show in Figure 57. Reflections off the wedged AR-coated surfaces tend to "walk off" without producing etalon effects. The HR coating, however, must be greater than 99.9% at 3.2 μm to achieve the required etalon Finesse. Contacted vendors believe they can produce this level of reflectivity.

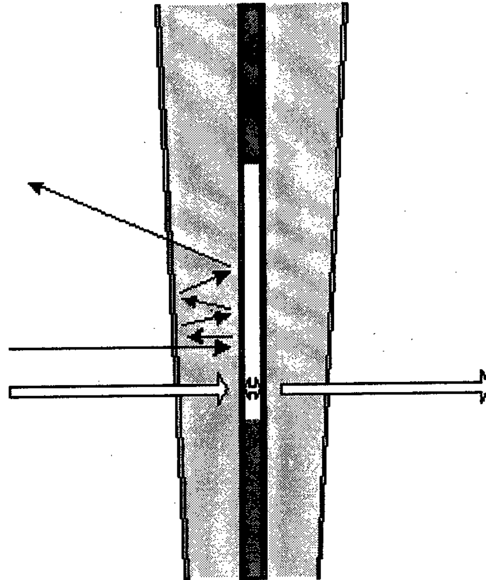

Figure 57. Fabricating the etalon with wedged substrates prevents cavity filter effects from other points in the construct. The white lines represent proper etalon transmission. The black lines show the lateral and angular drift of the beam when reflecting off the AR-coated surfaces.

The 15.5-μm air-gap cavity should be mounted at a 14.3° angle to produce at 16-μm-thick cavity. This avoids reflection problems that could occur if the assembled etalon is exactly perpendicular to the cavity beam. Less than 10° rotation of the etalon tunes the etalon transmission peak through the entire free spectral range.

External Cavity and Components

The external cavity was constructed from opto-mechanical components. Based upon an external cavity length of 8 cm, the design requires a Finesse for the etalon cavity of several thousand. As discussed later, such a high Finesse is very difficult to achieve. One factor, which can reduce the high Finesse requirement, is reducing the external cavity length. Some design adjustments have reduced the external cavity length (on paper) to 3 – 3.5 cm. Figure 58 shows the diagram of the external cavity with the actual dimensions for the various opto-mechanical components. This does not include the increased optical path length due to the index of the etalon substrates and the SOA. The opto-mechanical components and optics for the external cavity were purchased. The entire external cavity was built on a 1 x 2 ft^2 optical breadboard to allow easy transport to the Naval Research Laboratory for testing.

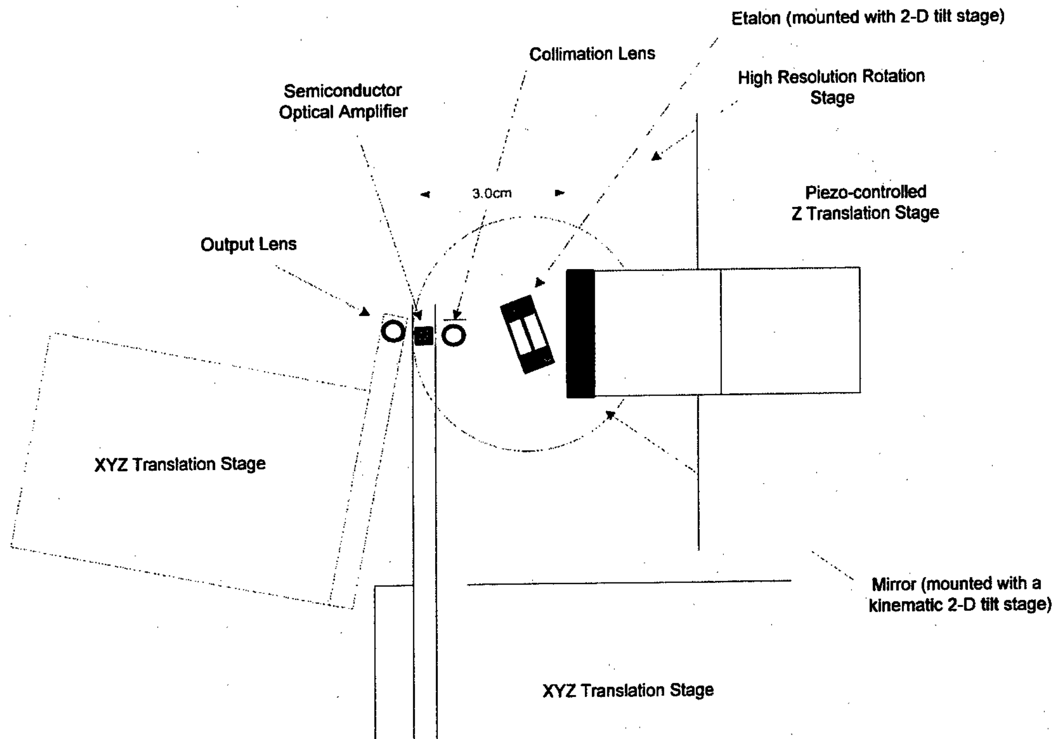

Figure 58. External Cavity Design (Note: all components are to scale except the SOA and lenses which are shown larger to be easily discernable).

The tuning etalon is an air-gap between two silicon wafers. In order to produce the high Finesse etalon needed, F > 1000, the silicon was coated with a very high reflectivity coating to produce the mirrors. To achieve such a high Finesse, the etalon mirrors must be extremely flat, less than 100 nm variation within the beam area of a few µm. While this degree of flatness has been achieved in other materials, such as BK7 glass, there has been very little demand from industry for silicon of this flatness.

Polishing the wafer was performed at Sarnoff. The polishing used a special, harder pad that produced greater flatness. The Si material to be used as the etalon was cut out from the center of the wafer, where it is flattest. Using a harder polishing pad makes polishing more difficult, but still possible, to produce a low scratch density and few dig figures. The polishing has been tested and appears to be adequate. The two surfaces were angle polished to prevent additional intracavity effects.

After polishing, the wafers were antireflection-coated with a broad band, 3 – 5 µm high reflectivity coating on one side and an anti-reflection coating on the other.

The highest quality mirrors require a substrate with a maximum 5:1 aspect ratio to remain flat. In order to reduce the thickness of the substrate, the lateral dimensions of the etalon was reduced from a 25-mm square to a 15-mm square. Still, a 3- to 4-mm-thick substrate would be required. With two of these mirrors within the cavity, and an index of refraction of 3.43 for silicon, this increases the cavity length by about 20 mm. Using a lower index substrate in place of silicon was investigated, but the alternatives are softer materials that are

more difficult to polish to a flat finish. By using a slightly lower reflectivity mirror, still > 99.7%, the substrate can be reduced to 1 to 2 mm thickness. This increases the cavity length by only 8 mm.

The 15.5-μm spacer layer was produced with spin-on resist. Two technologies were investigated. The first is spin-on photoresist. Spinning on a single layer of photoresist Futurrex NR5-8000, a thick photoresist, could achieve the desired thickness, but it varied radially at the slow spin speed. Uniformity was improved to +/- 0.5 μm over the 3" wafer by spinning on two coatings at higher speed with a short bake in between, being flattest near the center. Another potential spin-on material is BCB, Benzocyclobutene. BCB is commonly used for planarization and spinning on three layers should produce a very uniform 15.5 μm layer. Both spin-on resists are photosensitive. Following the spin-on and bake process the wafer is optically patterned to produce the windows for the etalon cavity and the avenues for dicing. The mask to pattern the wafers was designed and fabricated. Figure 59 shows the mask design.

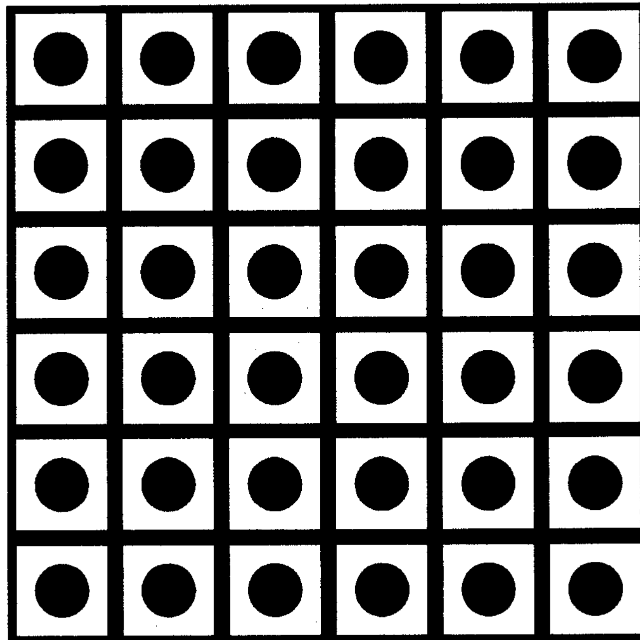

Figure 59. Etalon mask showing the round windows for the optical cavity and the avenues for sawing the wafer.

Cavity collimating lenses were sent to an outside vendor for AR-coating for 3.2-um. Components were received back from vendor. A Littrow grating was also received. Grating tuning of the cavity provides an alternative to etalon tuning, which is used to test the external-cavity initially. The tuning etalon provides better mode selectivity.

Coarse-Tuning Etalon Measurements

An alternate construction method for the tuning etalon was investigated to reduce the time and expense of experimenting with the assembly. Rather than spinning on photoresist, which restricts experimentation with each wafer, very thin films were considered. Thin-film sheets of polycarbonate (14 μm thickness) and polyimide (15 μm thickness) were acquired.

Using thin films allows more flexibility experimenting with the coated etalon mirrors, spacer layer, and mount.

An etalon clamp was designed and fabricated. The clamp was designed to hold the pieces of the silicon-based mirrors and the spacer together with an aperture for the collimated beam. The clamp was constructed of two stainless steel plates with four tightening screws, one at each corner. A soft material, such as a rubber o-ring, was used to protect the mirrors from the plates.

Two silicon wafers were polished and then coated with a broad band, 3 – 5 μm high reflectivity coating on one side and an anti-reflection coating on the other. These wafers were then diced into 15 x 15 mm^2 squares. Before dicing, the wafers were coated with photoresist to protect the surfaces from damage. Following the dicing, the photoresist was removed and the surface cleaned. Sandwiching a thin film spacer between two silicon squares with high reflectivity sides facing inward assembles an etalon. An aperture must be left open in the absorptive spacer material. Figure 60 shows the etalon clamp assembly.

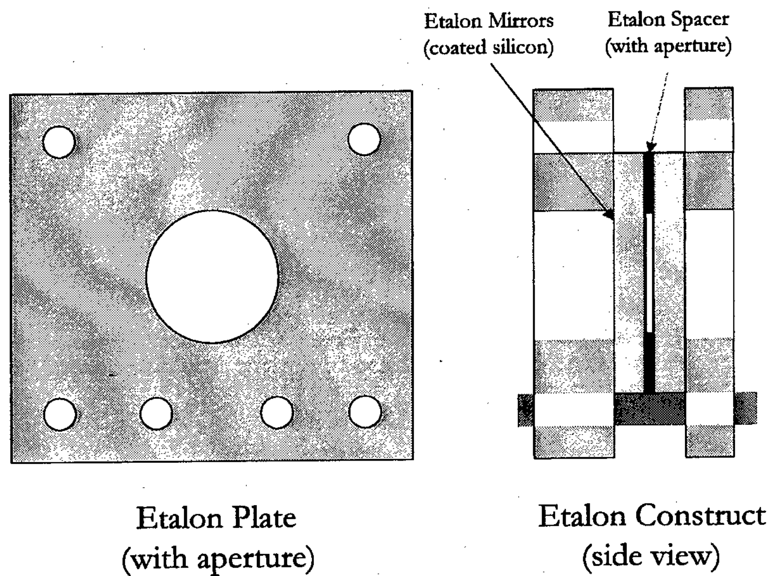

Figure 60. Tuning etalon clamp design.

After experimenting with polyimide and polycarbonate film tuning etalons were finally assembled with a polycarbonate spacer. Polycarbonate was generally easier to handle. Fourier Transform Infrared Spectroscopy (FTIR) measured the transmittance of these etalons. The screws on the clamp were adjusted to achieve parallelism between the mirrors of the etalon. It proved more difficult than expected to optimize the mirror parallelism due to the lack of real-time feedback during adjustment. The etalon had to be removed from the FTIR for adjustment, and each scan took a few minutes to complete. Figure 61 shows transmittance versus wavelength for a test tuning etalon. While the transmittance peaks are weak, they are periodic with wavenumber over the relevant range (approximately 2000 – 3500 cm^{-1}, or 3 to 5 μm, as shown in Figure 61). For an air-gap spacing between the mirrors, transmission peaks occur at resonance frequencies when

$$\frac{\lambda}{2}n = L$$

where L is the cavity length and n is an integer. Solving for the wavelength peaks with successive integers, one can calculate the etalon thickness. The peaks in Figure 62 correspond to a spacer thickness of 16.5 μm with a standard deviation of 0.1 μm.

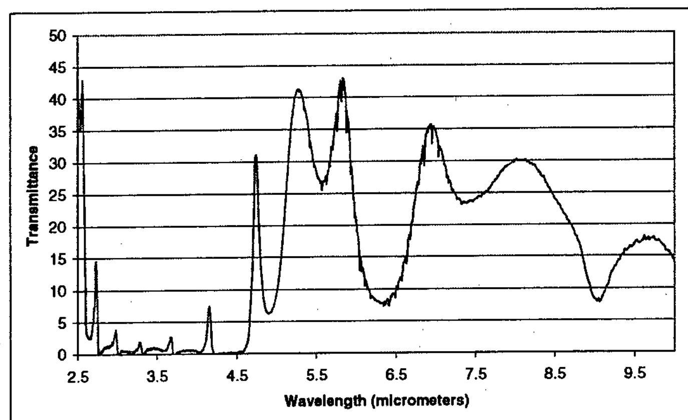

Figure 61. FTIR transmittance spectrum of a tuning etalon with a polycarbonate spacer. FTIR resolution is 2 cm^{-1}.

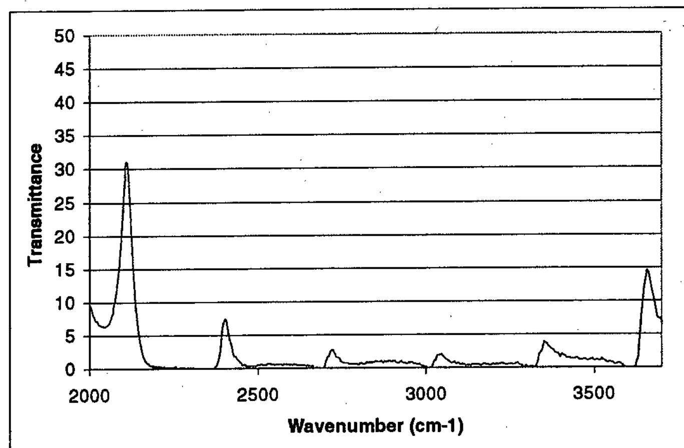

Figure 62. FTIR transmittance versus wavenumber of an etalon with polycarbonate spacer. FTIR resolution is 2 cm^{-1}.

Figure 63 shows an etalon spectrum for which the etalon mirrors were more nearly parallel. The resonances are sharper and the peak transmissions are higher.

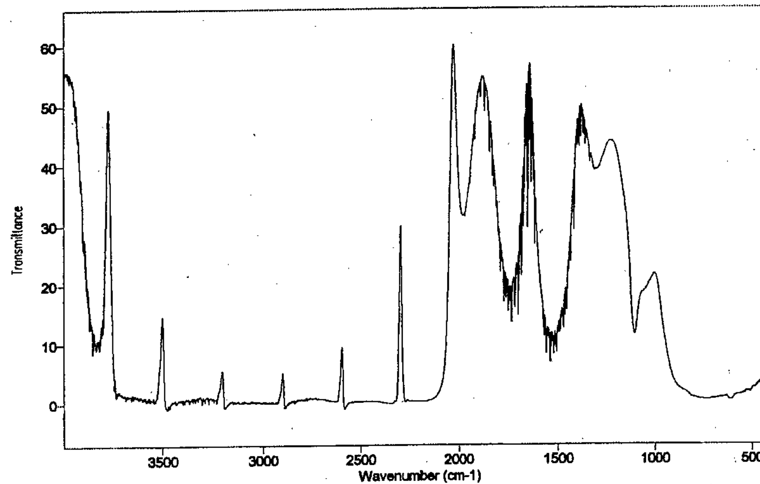

Figure 63. Etalon transmission spectrum similar to those in Figures 61 and 62, but with mirrors adjusted to be more nearly parallel.

The etalon air gap can be determined from a plot of the etalon peak transmission location in wavenumber, w, as a function of the number of half-wavelengths n of light resonating within the etalon (see Figure 64).

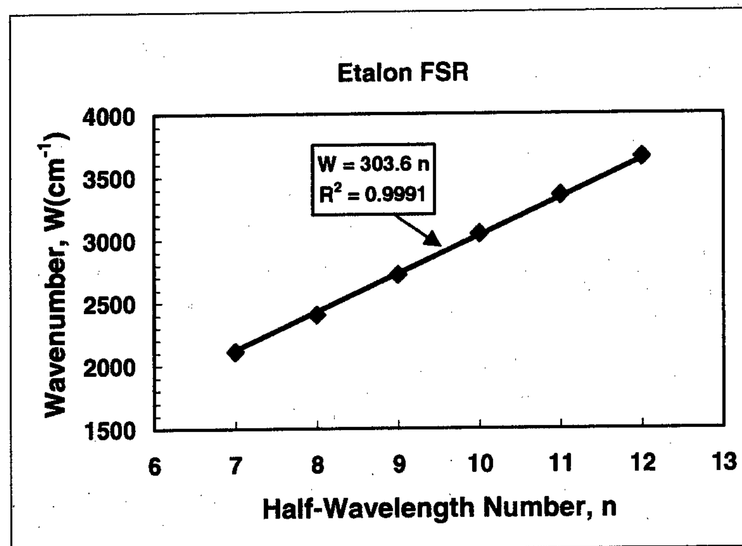

Figure 64. Least-squares fit of etalon peak-transmission wavenumber versus half-wavelength number.

A least-squares fit to the data in Figure 64 gives a slope of 303.6 cm^{-1}, which equals $1/2L_c$. This means that $L_c = 16.5$ µm, as stated above.

Additional etalon mirrors, which were AR/HR coated after they were diced, were processed. Once the etalons were tuned to achieve a high Finesse in the clamp apparatus, we intended to explore using epoxy to permanently bond the etalon as tuned and then to remove it from the clamp. This would have allowed a shorter external cavity path length, improving ECL performance.

External Cavity Summary and Conclusions

Sarnoff designed and constructed an external cavity that was compatible with the use of our antimonide-based semiconductor optical amplifiers. The external cavity is 8 cm long, and the entire mechanical assembly has a footprint smaller than 1 ft^2. Sarnoff designed, fabricated and partially characterized the tuning etalon that selects a particular longitudinal mode of the cavity. The etalon is an air-gap etalon using wedge-polished crystalline silicon mirrors and a polycarbonate spacer ring. The 16.5-μm polycarbonate spacer gives a FSR of 9 THz, or about 300 nm at a wavelength of 3 μm, which is the estimated width of the semiconductor optical amplifier.

This type of external cavity in conjunction with an antimonide-based semiconductor optical amplifier should perform well as a compact, wavelength-agile, single-frequency laser source.

V. Summary

The goal of this project is to develop a 3- to 5-μm continuously tunable single-frequency laser source. Our approach uses an external cavity (EC) and various tuning elements in conjunction with a semiconducting optical amplifier (SOA) that provides two-pass optical gain. The SOA is an antimonide-based mid-infrared laser structure with one facet having a very low reflectance ($< 10^{-4}$). Separate SOA designs offered optical or electrical pumping to produce optical gain.

Optically pumped, amorphous silicon ridge-waveguide lasers were developed that could be used as curved ridge waveguide semiconductor optical amplifiers. This was done through the parallel effort of growing an optimal laser structure via molecular-beam epitaxy and through optimizing a ridge-waveguide design. The resulting lasers operated up to a temperature of 295 K with no sign of output power saturation or of a runaway in the threshold current. At 295 K they output 7 mW per facet. Comparison with a stripe laser in the same material suggested that a flaw in the placement of the ridge metal mask induced losses that increased the threshold pump power by an order of magnitude and similarly reduced the external efficiency. The flaw was an overlap of the metal onto the ridge that masked off pump light. The wavelength of this laser varied from 3.05 μm at 78 K to about 3.10 μm at 295 K. The lateral far field patterns for both 7-μm-wide and 12-μm-wide ridge-waveguide lasers were multi-lobed, indicating that the lasers were not operating in the fundamental lateral mode.

We had SOA designs using GaSb ridge-waveguides etched into the grown laser structure. These were midway through processing when the project ended.

The successful operation of the 3-um optically pumped ridge waveguide laser is partially due to the redesign of the ridge. This redesign placed a silicon-nitride/amorphous-silicon layer between the metal mask and the antimonide cladding layer of the laser. In this way any optical losses caused by the metal were reduced. The inadvertent overlap of the metal onto the ridge may have caused the low external efficiency, and hence, low output power of the laser. With a properly processed amorphous-silicon ridge-waveguide, this approach should produce efficient, mid-infrared semiconductor optical amplifiers for the external cavity laser.

Sarnoff designed and constructed an external cavity that was compatible with the use of our proposed antimonide-based semiconductor optical amplifiers. The external cavity is 8 cm long, and the entire mechanical assembly has a footprint smaller than 1 ft^2. Sarnoff

designed, fabricated and partially characterized the tuning etalon that selects a particular longitudinal mode of the cavity. The etalon is an air-gap etalon using wedge-polished crystalline silicon mirrors and a polycarbonate spacer ring. The 16.5-μm polycarbonate spacer gives a FSR of 9 THz, or about 300 nm at a wavelength of 3 μm, which is the estimated width of the semiconductor optical amplifier.

This type of external cavity in conjunction with an antimonide-based semiconductor optical amplifier should perform well as a compact, wavelength-agile, single-frequency laser source.

VI. References

1. R. U. Martinelli, D. Z. Garbuzov, H. Lee, P. K. York, R. J. Menna, J. C. Connolly, and S. Y. Narayan, "InGaAsSb/AlGaAsSb Mid-Infrared Diode Lasers for Gas Sensing", Proc. SPIE vol. **2382**, 250 (1995)
2. M. Phillips, "Breath Tests in Medicine", *Scientific American*, p. 74, July 1992
3. K. L. Moskalenko, A. I. Nadezhdinskii, I. A. Adamovskaya, "Human breath trace gas content study by tunable diode laser spectroscopy technique", Infrared Physics and Teechnology, **37**, 181 (1996)
4. D. E. Cooper, R. U. Martinelli, C. B. Carlisle, H. Riris, D. P. Bour, and R. J. Menna, "Measurement of $^{12}CO_2$:$^{13}CO_2$ ratios for medical diagnostics with 1.6-μm distributed-feedback semiconductor diode lasers", Applied Optics, **32**, 6727 (1993)
5. H. Lee, L. J. Olafsen, R. J. Menna, W. W. Bewley, R. U. Martinelli, I. Vurgaftman, D. Z. Garbuzov, C. L. Felix, M. Maiorov, J. R. Meyer, J. C. Connolly, A. R. Sugg, and G. H. Olsen, "Room-Temperature type-II W quantum well diode laser with broadened waveguide emitting at $\lambda = 3.3$ μm", Electron. Lett., **35**, 1743 (1999)
6. Gerald A. Alphonse, Dean B. Gilbert, M. G. Harvey, and Michael Ettenberg, "High-Power Superluminescent Diodes", IEEE J. Quantum Electron., **24**, 2454 (1989)
7. E. A. J. Marcatili, "Bends in Optical Dielectric Waveguides", Bell Syst. Tech. J., **48**, 2103 (1969)
8. E. A. J. Mercatili and S. E. Miller, " Improved Relations Describing Directional Control in Electromagnetic Wave Guidance", Bell System Tech. Journal, **48**, 2161 (1969)
9. D. Z. Garbuzov, R. U. Martinelli, H. Lee, P. K. York, R. J. Menna, J. C. Connolly, and S. Y. Narayan, "Ultralow-loss broadened-waveguide high-power 2 μm AlGaAsSb/InGaAsSb/GaSb separate-confinement quantum-well lasers", Appl. Phys. Lett., **69**, 2006 (1996)
10. W. W. Bewley, H. Lee, I. Vurgaftman, R. J. Menna, C. L. Felix, R. U. Martinelli, D. W. Stokes, D. Z. Garbuzov, J. R. Meyer, M. Mairov, J. C. Connolly, A. R. Sugg, and G. H. Olsen, "Continuous-wave operation of $\lambda = 3.2$ μm broadened-waveguide W quantum-well diode lasers up to T = 195 K", Appl. Phys. Lett., **76**, 256 (2000)
11. J. R. Meyer, C. L. Felix, W. W. Bewley, I. Vurgaftman, E. H. Aifer, L. J. Olafsen, J. R. Lindle, C. a. Hoffman, M.-J. Yang, B. R. Bennet, and B. V. Shanabrook, "Auger coefficients in type-II InAs/$Ga_{1-x}In_xAs$ quantum wells", Appl. Phys. Lett., **73**, 2857 (1998)
12. C. L. Felix, W. W. Bewley, E. H. Aifer, I. Vurgaftman, L. J. Olafsen, D. W. Stokes, J. R. Meyer, M. J. Yang, H. Lee, R. U. Martinelli, J. C. Connolly, A. R. Sugg, and G. H. Olsen,

"Optically Pumped Mid-Infrared Type-II Lasers: Advances in High-Temperature Performance", in In-Plane Semiconductor Lasers III, H. K. Choi and P. S. Zory, Editors, Proc. SPIE Vol. **3628**, 130 (1999)

13. M. J. A. de Dood, A. Polman, T. Zijlstra, and E. W. J. M. van der Drift, "Amorphous silicon waveguides for microphotonics", J. Appl. Phys., **92**, 649 (2002)
14. D. E Carlson and C. R. Wronski, Appl. Phys. Lett., **28**, 671 (1976)
15. G. Cocorullo, F. Della, R. DeRossa, I. Rendina, A. Rubino, and E. Terzini, IEEE J. Selected Topics in Quantum Elec., **4**, 997 (1998)
16. A. M. Argawal, L. Liao, J. S. Foresi, M. R. Black, X. Duan, and L. C. Kimerling, "Low-loss polycrystalline silicon waveguides for silicon photonics", J. Appl. Phys., **80**, 6120 (1996)